Supporting Information

Stable Ultra-Concentrated and Ultra-Dilute Colloids of $CsPbX_3$ (X=Cl, Br) Nanocrystals using Natural Lecithin as a Capping Ligand

Franziska Krieg,[†,‡] Quy K. Ong,[§] Max Burian,[&] Gabriele Rainò,[†,‡] Denys Naumenko, [¥] Heinz Amenitsch, [¥] Adrian Süess,[†,‡] Matthias J. Grotevent,[†,#] Frank Krumeich,[†] Maryna I. Bodnarchuk, [†,‡] Ivan Shorubalko,[#] Francesco Stellacci[§] and Maksym V. Kovalenko[†,‡*]

[†] Institute of Inorganic Chemistry, Department of Chemistry and Applied Bioscience, ETH Zürich, Vladimir Prelog Weg 1, CH-8093 Zürich, Switzerland

[‡] Laboratory for Thin Films and Photovoltaics, Empa – Swiss Federal Laboratories for Materials Science and Technology, Überlandstrasse 129, CH-8600 Dübendorf, Switzerland

[#] Laboratory for Transport at Nanoscale Interfaces, Empa – Swiss Federal Laboratories for Materials Science and Technology, Überlandstrasse 129, CH-8600 Dübendorf, Switzerland

[§] Institute of Materials, École Polytechnique Fédérale de Lausanne (EPFL), Switzerland

[&]Swiss Light Source, Paul Scherrer Institut, 5232 Villigen PSI, Switzerland

[¥]Institute of Inorganic Chemistry, Graz University of Technology, Stremayrgasse 9/V, 8010 Graz, Austria

1. Chemicals

The following reagents were purchased and used as received:
Cs_2CO_3, sulfobetaine-16 (3-(N,N-dimethylhexadecylammonio)propanesulfonate, ASC16) and 1,3-propanesultone were purchased from Fluorochem, sulfobetaine-8 (3-(N,N-dimethyloctylammonio)propanesulfonate, ASC8), sulfobetaine-12 (98%, 3-(N,N-dimethyldodecylammonio)propanesulfonate, ASC12), soy-lecithin (>97%, biochemistry grade) from Roth, potassium permanganate from Fluka, lead acetate trihydrate (99.99%), bromine (99.9%), formaldehyde (37% in water), formic acid (puriss), ethanol (analytical grade), HCl (fuming), 1-octadecene (ODE, technical grade), iso-propanol (puriss), 3-(N,N-dimethyloctadecylammonio)propanesulfonate (>99% , ASC18), oleic acid (90%, OA) and DMSO-d^6 from Sigma Aldrich/Merck, toluene (for synthesis), acetone (HPLC grade), acetonitrile (HPLC grade) from Fischer and trioctylphosphine (>97%, TOP), oleylamine (>95%, OLA) and C_6D_6 from STREM. 3-(N,N-Dimethyloleylammonio)propane sulfonate ("oleyl-sulfobetaine") was prepared according to our previous report [1].

2. Modelling

Colloidal stability is achieved in those systems, where the Brownian motion outcompetes gravitation. Loss of colloidal stability in time is due to aggregation, which can be described as a bimolecular reaction with an effective activation barrier composed of Van der Waals attraction (E_{VdW}), electrostatic repulsion (E_{El}), and steric forces (E_{Steric}). In the following we will consider charge neutral NCs of identical size (7 nm) and composition ($CsPbBr_3$), therefore the only force distinguishing the systems is the steric interaction.

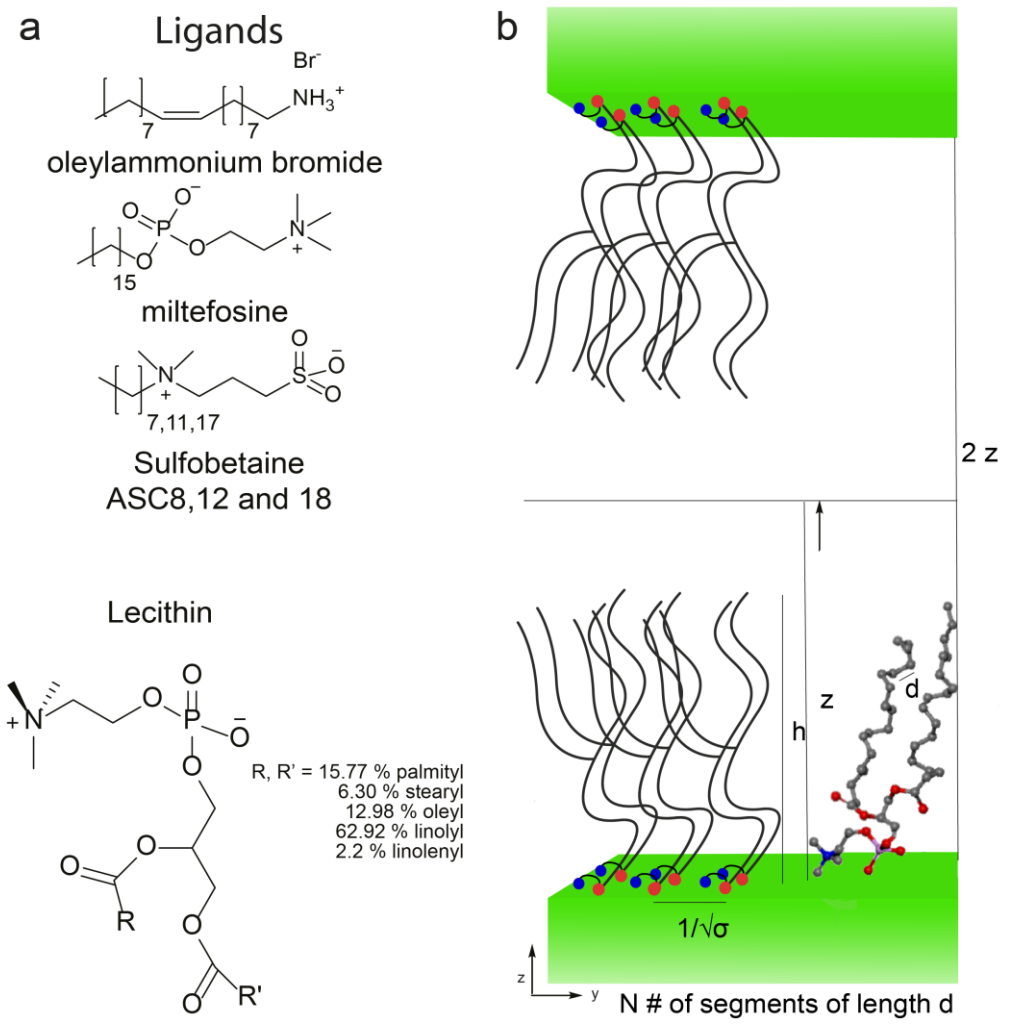

Figure S1. (a) Molecular structures of ligands modelled. (b) Sketch of the brush interaction, indicating variables used in the equations.

Steric stabilization of colloidal NCs is based on the competition of volume exclusion, which is driven by maximizing the entropy of the surface ligands and the osmotic potential, which is driven by minimizing the enthalpy of the system by increasing favorable ligand-solvent interactions. A force balance approach for these two countercurrent effects was proposed by Alexander and De Gennes [2] and further improved and generalized by Milner et al. [3] and since found to well agree with both computational [4] and experimental results [3c, 5]. The equation below is valid for stretched "polymer" chains, in this case up to 23 units, which are irreversibly grafted to an infinite, flat, solid, impenetrable substrate, as depicted in Figure S1 along with the molecular structures of all ligands considered. The surface of the NC is indeed flat due to their cuboidal shape. Surface infinity is an acceptable assumption for relatively large cuboidal NCs. It is further assumed that the grafting is irreversible (stable) for the case of zwitterionic ligands [1], and highly dynamic for OA/OLA ligands [6]. The properties that we calculate for a permanently attached brush can also be calculated for the dynamic case [2b] if the magnitude of the activation energy and molecular mechanism of the attachment and detachment are known. The assumption of stretched polymers is met as soon as the grafting density overcomes the square root of the chain contour length [7]. An additional assumption required by this model is that the brushes of different NCs don't interpenetrate when compressed. Inherent to this argument is that the van der Waals forces between ligands of opposite surfaces will not be different from the van der Waals forces between ligands on the same surface and that the van der Waals interactions are not chain length dependent. This argument, while usually true for polymers, can be questionable for short oligomers [8]. This leads to a qualitative overestimation of the energy of repulsion for long saturated chains. Such influences can be minimized practically by disfavoring the bilayer formation of opposite surface ligands by the introduction of cis double bonds (see Figure S3) or short side chains [8-9].

The energy of repulsion was calculated by numeric integration over the inter-particle distance of the pressure given in equation (1). Where A denotes the surface area, k_B is the Boltzmann constant, T is the temperature, N is the number of rigid monomer units (CH_2-units in the present case), d is the size of a monomer, w is the excluded volume parameter (monomer-monomer repulsion factor), σ is the grafting density (ligands per unit area), h is the brush thickness and $2z$ is the distance between two flat surfaces.

$$\frac{F_{Steric}}{A} = \frac{k_B T\, N\, d^2 \sigma}{h}\left(\frac{\pi^2}{12}\right)^{\frac{1}{3}} (\sigma d^2 w)^{2/3} \int_0^h \frac{1}{2}(h/z)^2 + \frac{1}{2}(z/h)^4 - \frac{z}{h} dz \tag{1}$$

The expression for the brush height h is given in equation (2).

$$h \sim N d^2 (w \sigma d^2)^{1/3} \tag{2}$$

From equation (1) it is appreciable that improved colloidal stability will be reached for higher grafting density and longer and less compressible chains. The excluded volume parameter w is mostly constant between the systems considered and was not used as a free variable. The highest saturation concentrations in the experiment were reached using soy lecithin as a ligand. Due to its biological origin, it is the physiological mixture of molecules with different chain lengths. This demands for an extension of the brush- model to poly-dispersed chains. The model is a superposition of several monodispersed brushes [10].

$$\frac{F_{steric}}{A} = k_B T\left(\frac{\sqrt{2}}{\pi}\sum_i \int_0^h (Mw_i - Mw_{i-1})\sqrt{U(z) - U_{i-1}(z)}\,\theta(i) dz - z\right)^{2x/(x+3)} \qquad x \geq 3 \tag{3}$$

New variables introduced are: Mw_i the molecular weight of a chain i, $U(z)$ the monomer distribution in the brush as a function of the distance from the surface, which is commensurate with the expression used for monodispersed chains and $\theta(i)$ the statistical occurrence of a chain i. In accordance with our experimental results, polydispersity increases the steric stabilization. All of these models are self-consistent, meaning that the results while qualitatively accurate will have no quantitative relevance. The variables are chain length and grafting density. The chain length is known and the grafting density can be determined by either TGA or NMR (see table S2). The brush height was also modelled with molecular mechanics simulations and showed to be qualitatively consistent with the values received by self-consistent mean field theory. Also, a parabolic density profile was generally reproduced (Figure S2).

Table S1. Brush height calculations from self-consistent mean field theory and molecular mechanics.

Ligand	h-mean field theory (Å)	h-molecular mechanics (Å)	Experimental grafting density (%)	Contour length (Å)
OA/OLA	<15.9	18.4	79	27.5
Miltefosin	13.6	16.6	-	24.5
ASC8	6.8	9.4	-	12.3
ASC12	9.3	13.8	56	18.5
ASC16	14.0	15.7	72	24.6
ASC18	15.7	19.8	72	27.7
All stearyl lecithin	22.5	28.3	-	32.1
All oleyl lecithin	22.1	26.0	-	32.3
lecithin	17.4	-	64	32.0

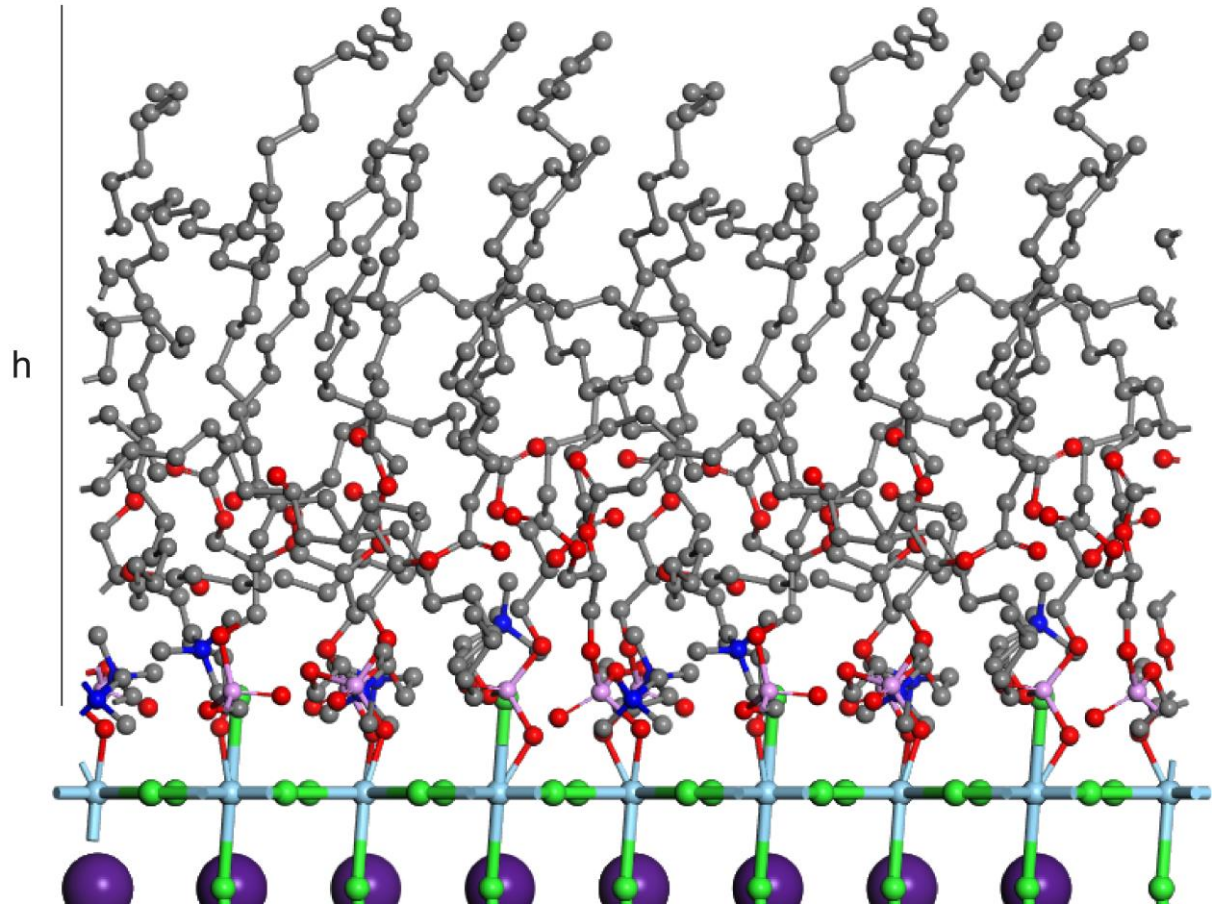

Figure S2. Molecular mechanics model for all stearyl lecithin (1,2-distearoyl-*sn*-glycero-3-phosphocholine).

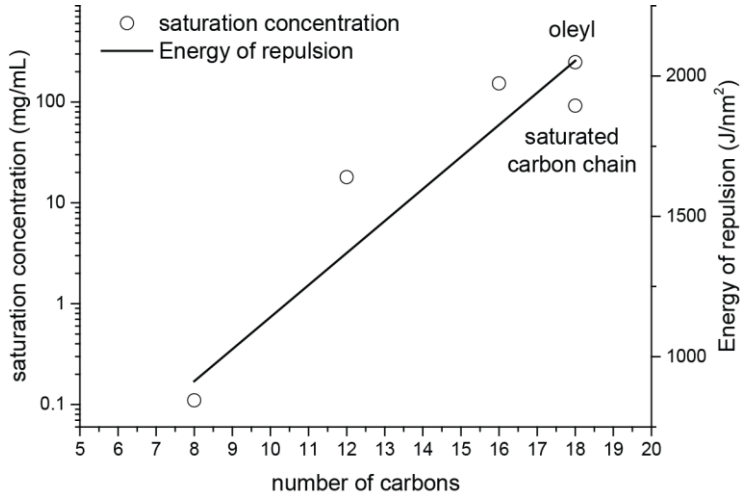

Figure S3. Dependence of the saturation concentration on the sulfobetaine chain length. We note that the deviation from the logarithmic behavior predicted by theory can be due to the interpenetration of the brushes, leading to a gain in either enthalpy (attractive van der Waals forces) or entropy (crystallization and therefore solvent elimination). These types of interactions are not included in our model. The effect can be seen most clearly in the saturated 18-carbon chain, which yields, contrary to the predicted trend, a smaller saturation NC concentration than its C16 analog. To mitigate this difference of enhanced crystallization of neighboring brushes, the oleyl (unsaturated) equivalent of the ligand was used and gave the result within the expected trend.

2.1 Molecular mechanics model

$CsPbBr_3$ surfaces were cut out of a bulk crystal with the crystal structure (P*bnm*) published for the NCs [11]. The slab was terminated by the CsBr (001) plane and pairs of Cs and Br were replaced by the tested molecules. Pb, Br, and Cs positions were constrained during all structure relaxations. The unit cell was enlarged to 80 Å on the side of the $CsPbBr_3$ slab where the ligands shall be attached. Phosphonate groups were set to bind Pb atoms. The nitrogen-surface distance was relaxed using *Forcite* and the universal force field, electrostatic interactions were included and charges were set to the thermodynamically most stable values. Once a stable configuration was found, the z-coordinates of the binding groups were constrained as well and the charges were all set to 0. The brushes were relaxed as they were and in the presence of toluene at its bulk density. The brush height was measured as the vertical distance between the furthest atom of the brush and the surface. Values are given in Table S1.

2.2 Comparison to experimental data

The saturation concentration is the lowest concentration at which the NCs are not completely dispersible. The excess NCs were removed from the solution by centrifugation and the concentration of the saturated solution was determined using the method of Maes *et al.* [12] based on the known optical absorption coefficients of $CsPbBr_3$ NCs at 335 nm. At this photon energy, the volumetric absorption coefficient is NC-size-independent. NCs were suitably diluted, typically by a factor of 3000, before recording the absorption spectra. The purity of NCs was monitored by NMR. TGA was used to estimate the content of ligands and hence the ligand coverage, using the NC size information from TEM (see Table S2).

Table S2. Summary of NMR, TEM, DLS and TGA data.

Sample	Diffusion coefficient ($m^2/s\ 10^{-9}$)	Estimated diffusion coefficient ($m^2/s\ *10^{-9}$)	Estimated size from DOSY (nm)	Measured size TEM (nm)	Measured size DLS (d.nm)	Ligand mass fraction (%)	Coverage (nm^{-2})	Ref.
benzene	1.93	-	-	-	-	-	-	[1]
OLAmBr	0.361	-	-	-	-	-	-	[6]
OA/OLA covered NCs	0.166	-	3.7	8.4	-	-	2.3 (79%)	[6]
sulfobetaine (ASC18)	0.68	-	-	-	-	-	-	[1]
ASC18-covered NCs	0.0541	0.0609 ±0.0110	10.1	9 ± 2	-	20% in 8 nm NCs	2 (72%)	[1]
oleyl-sulfobetaine		-	-	-	-	-	-	
oleyl-sulfobetaine covered NCs	0.0480	0.0609 ±0.0110	11.4	9 ± 2	14 ± 3	13% in 13.9 nm NCs	2.15 (72%)	[1]
lecithin in benzene (micelles)	0.097	-	-	-	-	-	-	this work
lecithin in DMSO/benzene (no micelles)	0.18-0.46	-	-	-	-	-	-	this work
lecithin-covered NCs	0.0425	0.0498 ±0.0182	12.9	-	11 ± 3	-	-	this work
lecithin-covered NCs	0.042	0.0784 ±0.0098	13	7 ± 1	-	26	1.8 (64%)	this work

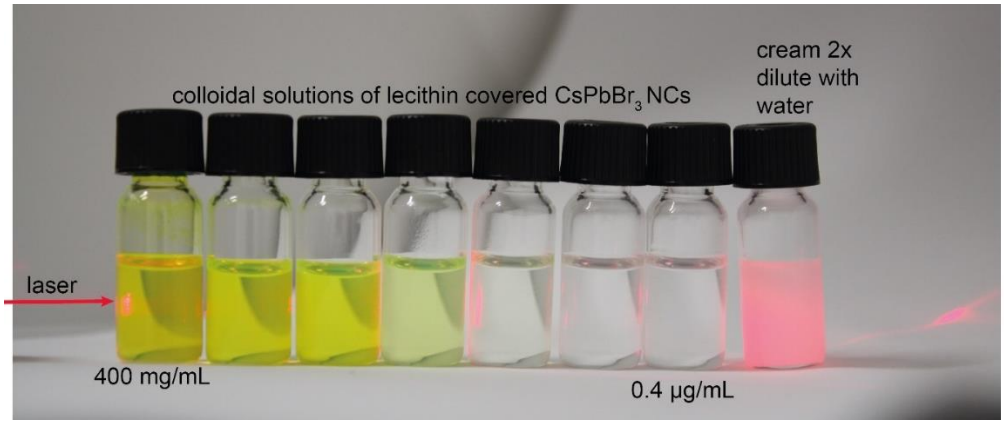

Figure S4. The absence of Tindall effect on colloidal solutions of lecithin-covered $CsPbBr_3$ NCs at all concentrations and its strong manifestation in the oil-in-water emulsion (diluted milk cream). Concentration decreases left to right by the factor of 10 between neighboring vials.

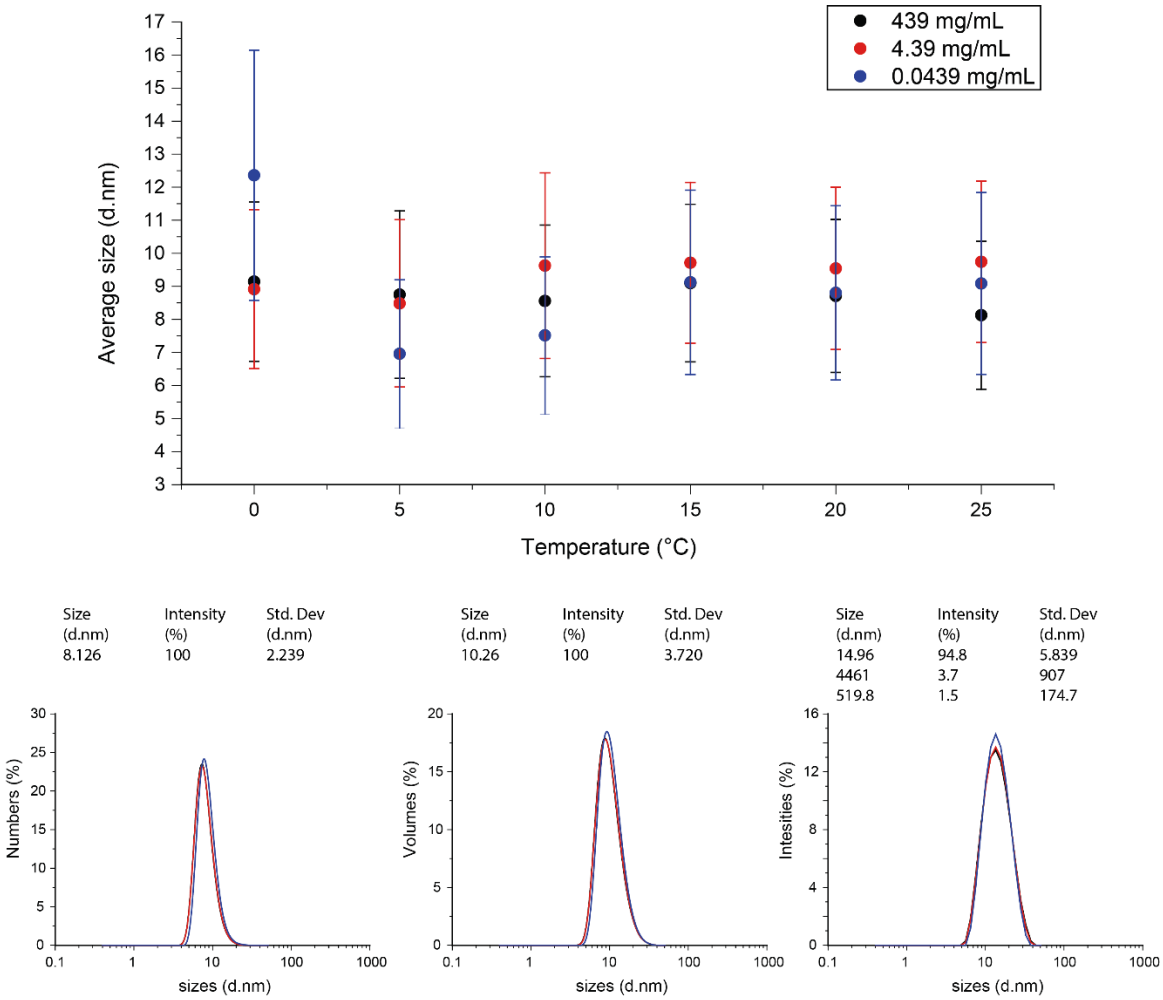

Figure S5. DLS data obtained from a lecithin-covered $CsPbBr_3$ sample at different concentrations and temperatures. On the bottom the intensity, volume and number averages are plotted for the highest concentration at room temperature. Each measurement was repeated 3 times, indicated by the three curves. The sizes received by DLS agree well with the ones received by TEM and DOSY NMR. As it can be seen from the different processing modes of the DLS measurements, colloids are aggregate-free. Furthermore, lecithin-covered $CsPbBr_3$ NCs 439 mg/mL remain dispersed completely upon centrifugation at 29500 g for 1 hour. They cannot be filtered at such concentrations due to crowding of the filter. If diluted 300 times, filtration is, however, possible with a 0.45 μm pore syringe filter.

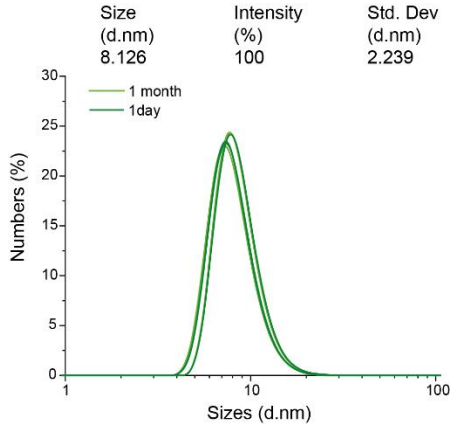

Figure S6. DLS of lecithin-covered $CsPbBr_3$ at a concentration of 419 mg/mL after 1 day and after 1 month. The measurement was repeated 3 times each time. Good match of these curves indicates the retention of the colloidal state and NC dimensions; within the DLS accuracy.

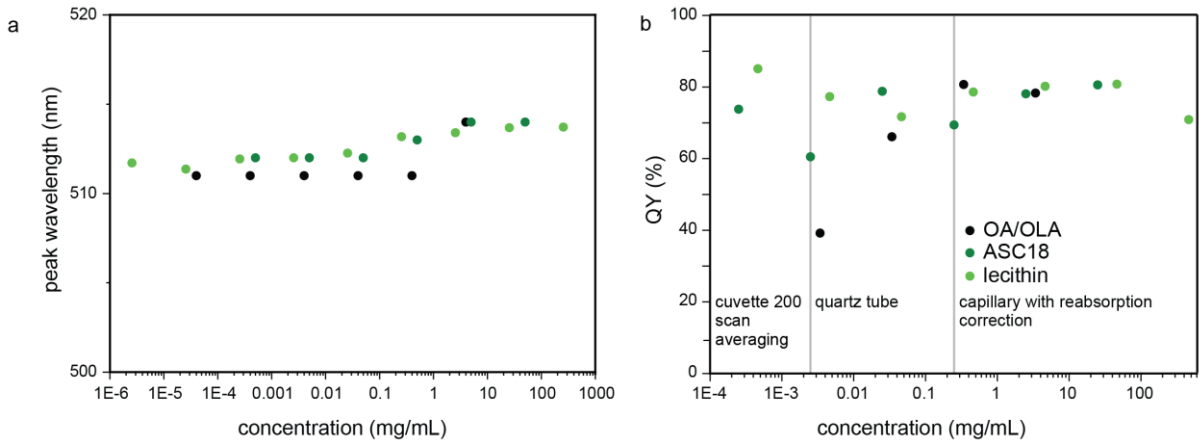

Figure S7. (a) No substantial PL peak shift can be seen in sulfobetaine-capped and lecithin-capped NCs upon dilution over 9 orders of magnitude. A few-nm-longer PL peak in concentrated NCs is due to re-absorption effect. (b) Absolute QY as a function of dilution for $CsPbBr_3$ capped with different ligands.ASC18-capped NCs are robust against dilution down to 10^{-6} mg/mL, while OA/OLA capped NCs start to decompose for concentrations below 1 mg/mL. Lecithin-capped NCs are stable up to concentrations as high as 400 mg/mL (inorganic content), whereas ASC18-capped NCs exhibit saturated concentration of up to 90 mg/mL.

3. Synthesis procedures

3.1 Cs-oleate 0.4 M in ODE

Cesium carbonate (1.628 g, 5 mmol), oleic acid (5 mL, 16 mmol) and 1-octadecene (20 mL) were evacuated at 25-120 °C until the completion of gas evolution.

3.2 Pb-oleate 0.5 M in ODE

Lead (II) acetate trihydrate (4.607g, 12 mmol), oleic acid (7.6 mL, 24 mmol) and 1-octadecene (16.4 mL) were mixed in a three-necked flask and evacuated at 25-120 °C until the complete evaporation of acetic acid and water.

3.3 TOP-Br_2 0.5 M in toluene

TOP (6mL, 13 mmol) and bromine (0.6 mL, 11.5 mmol) were mixed under inert atmosphere. Once the reaction was complete and cooled to room temperature, the TOP-Br_2 was dissolved in toluene (18.7 mL).

3.4 TOP-Cl_2 0.5M in toluene

TOP (30 mL, 0.067 mol) was reacted with Cl_2 gas (ca. 0.34 mol, *i.e.* large excess) at 0 °C. Chlorine gas was produced in-situ by the reaction of concentrated HCl (85 mL, 0.6725 mol) and potassium permanganate (106.27 g) and, after being cleaned from residual HCl by water, was transferred to the reaction vessel by argon gas flow. The resulting transparent product was diluted with toluene (93 mL).

3.5 Nanocrystals $CsPbX_3$ (X=Br, Cl and their mixtures) with lecithin as a ligand

In a typical synthesis of $CsPbX_3$ NCs, Cs-oleate (4 mL, 1.6 mmol), Pb-oleate (5 mL, 2.5 mmol) and lecithin (0.324 g, *ca.* 0.45 mmol) were dissolved in ODE (10 mL) and heated under vacuum to 80-150 °C, whereupon the atmosphere was changed to argon and TOP-X_2 in toluene (5 mL, 5 mmol of X) was injected. The reaction was cooled immediately by an ice bath. NC size can be controlled by increasing temperature for adjusting the NC size in the range of 6 -10 nm (492-515 nm for $CsPbBr_3$, see Table S3 and Figure S15).

Isolation and purification. The crude solution was precipitated by the addition of 2 volumetric equivalents of acetone, followed by the centrifugation at 29500g (g is the earth gravity) for 10 minutes. The precipitated fraction was dispersed in 10 mL of toluene and then washed three more times. Each time the solution was mixed with two volumetric equivalents of acetone and centrifuged at 29500 g for 1 minute, and subsequently dispersed in the progressively smaller amounts of the solvent (5mL for the second cycle, 2.5 mL for the third cycle). After the last precipitation, NCs were dispersed in 2 mL of toluene and centrifuged at 29500 g for 1 minute to remove any non-dispersed residue.

Size selection (instead of isolation) and purification. In order to obtain monodisperse fractions, size selection was performed by the gradual addition of acetone to the crude solution in small portions, each time isolating a fraction of the NCs by centrifuging (at 29500 g for 10 minutes). The portion of the acetone is chosen each time such that it is minimally sufficient to induce an observable flocculation of the NCs (seen as a noticeable but small turbidity). First additions of acetone destabilize the largest NCs, whereas smallest NCs constitute later fractions.

Typically, with the entire crude solution (~25 mL), it requires 8-20 mL (less for higher synthesis temperature) of acetone to induce noticeable turbidity and hence isolate a first fraction. Subsequent acetone portions typically are 0.5-2 mL. The total volume of a anti-solvent added was ca. 45-50 mL (*i.e.* twice the volume of the crude solution). Further addition of acetone typically did not cause further flocculation of NCs. Each fraction can be dispersed in toluene and further purified as described in the previous section. The result of this size-selective precipitation performed on a batch prepared at 130 °C can be seen in Figure 3. NCs with other ligands (OA/OLA, ASC18, ASC16, ASC12, ASC8, miltefosine) were synthesized according to our previously published procedures.[1, 13]

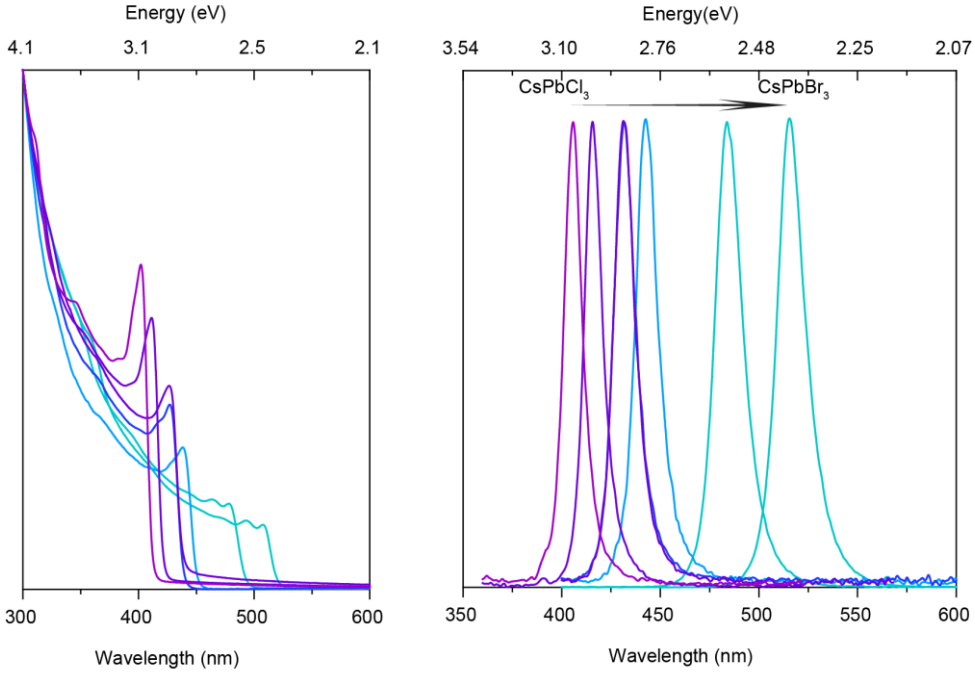

Figure S8. Color tunability by synthesis mixed-anion solid-solutions $CsPb(Cl/Br)_3$ NCs. The end-spectra correspond to monohalide compositions; *i.e.* $CsPbCl_3$ (407 nm) and $CsPbBr_3$ NCs (518 nm). Formation of bromide-iodide solid solutions had not been successful.

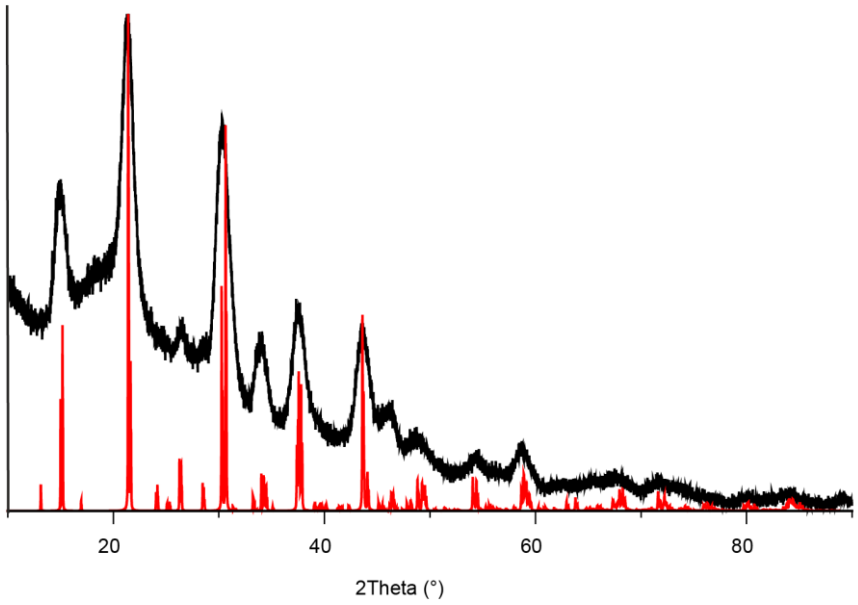

Figure S9. Powder XRD of lecithin-covered $CsPbBr_3$ NCs prepared at 130 °C, along with P*bnm* $CsPbBr_3$ reference (red) [11, 14].

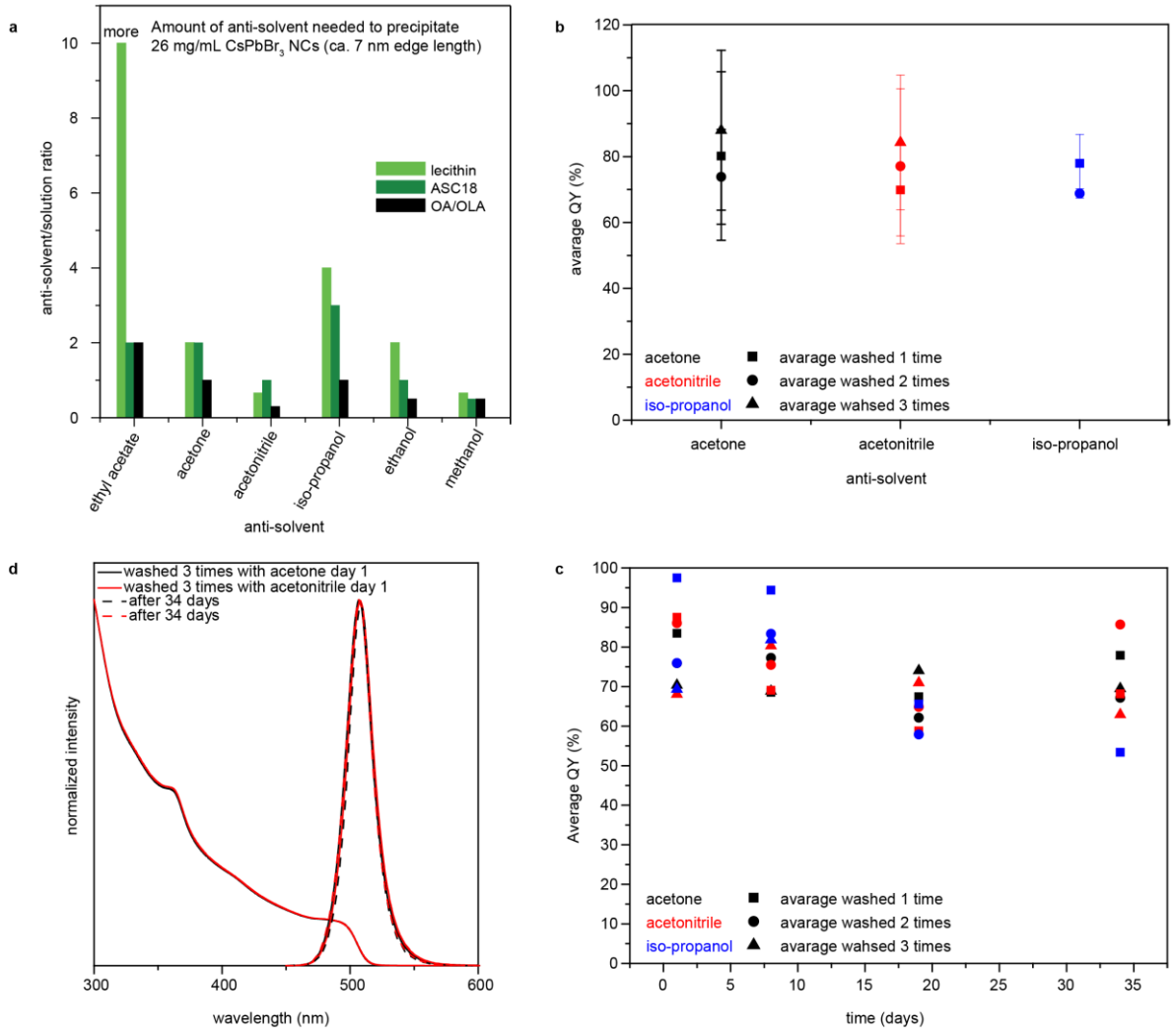

Figure S10. Stability tests for lecithin-covered $CsPbBr_3$ NCs. (a) Typical antisolvent-to-solvent volume ratios needed for the complete precipitation of NCs from their toluene solutions (26 mg/mL $CsPbBr_3$-NCs for lecithin- and ASC18-capped NCs, *ca.* 7 nm edge length) covered with different ligands. Concentrations in OA/OLA NCs were below 10 mg/mL as higher concentrations are not colloidally stable. Ethyl acetate does not precipitate the lecithin-capped NCs at 26 mg/mL. The results are in good agreement with the trend seen in the saturated concentrations (Figure 1c) and calculated ligand repulsion potentials. (b, c) Acetone, acetonitrile and *iso*-propanol were chosen for further purification studies. The quantum yields are retained after at least three rounds of precipitation and redispersion and for at least 34 days. (d) No significant change in the absorption or luminescence spectra can be noticed upon purification and prolonged storage.

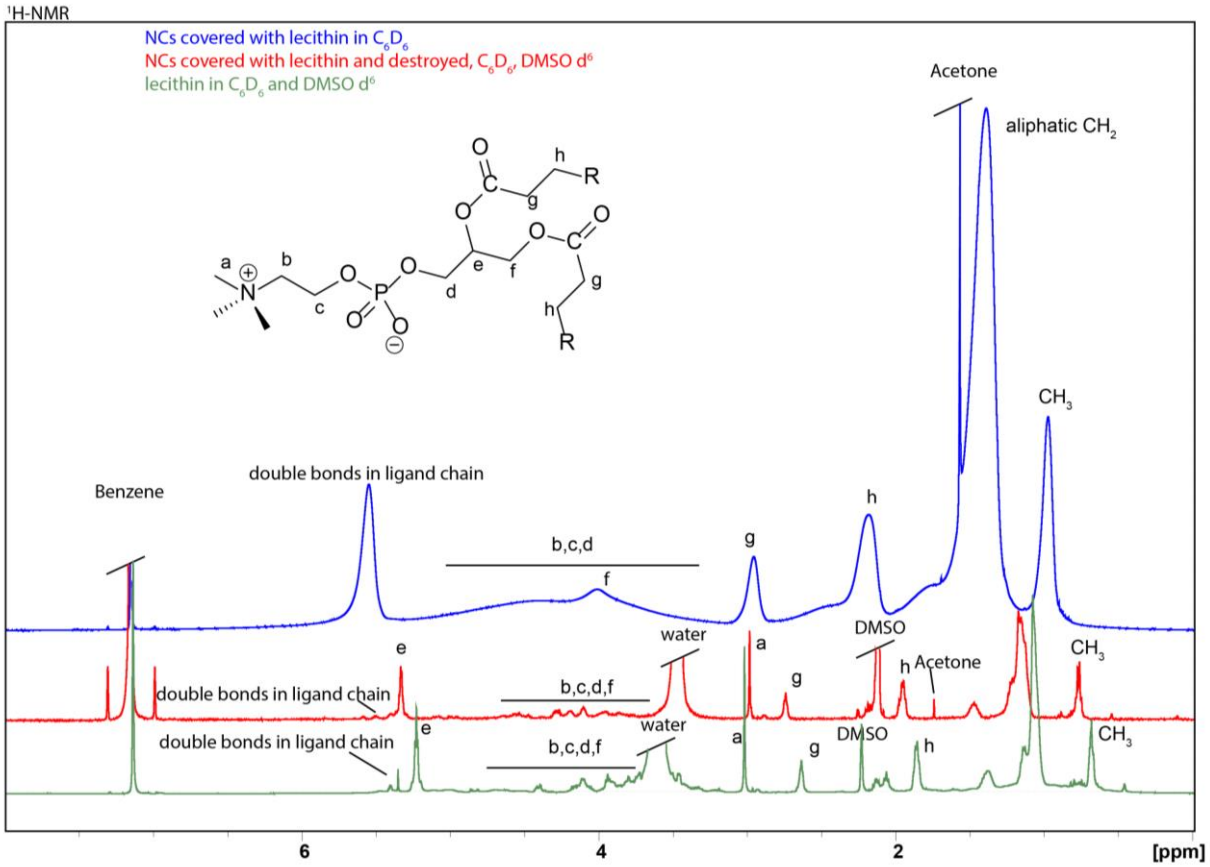

Figure S11. [1]H NMR of lecithin (green) and lecithin-covered NCs before (blue) and after dissolution (red, disintegration of NCs) in d[6]-DMSO. Peaks common to all lecithin components were assigned according to the general pictogram. Presence of oleic acid or oleate cannot be ruled out, but should be minimal in accord with our earlier results on sulfobetaine-capping.[1]

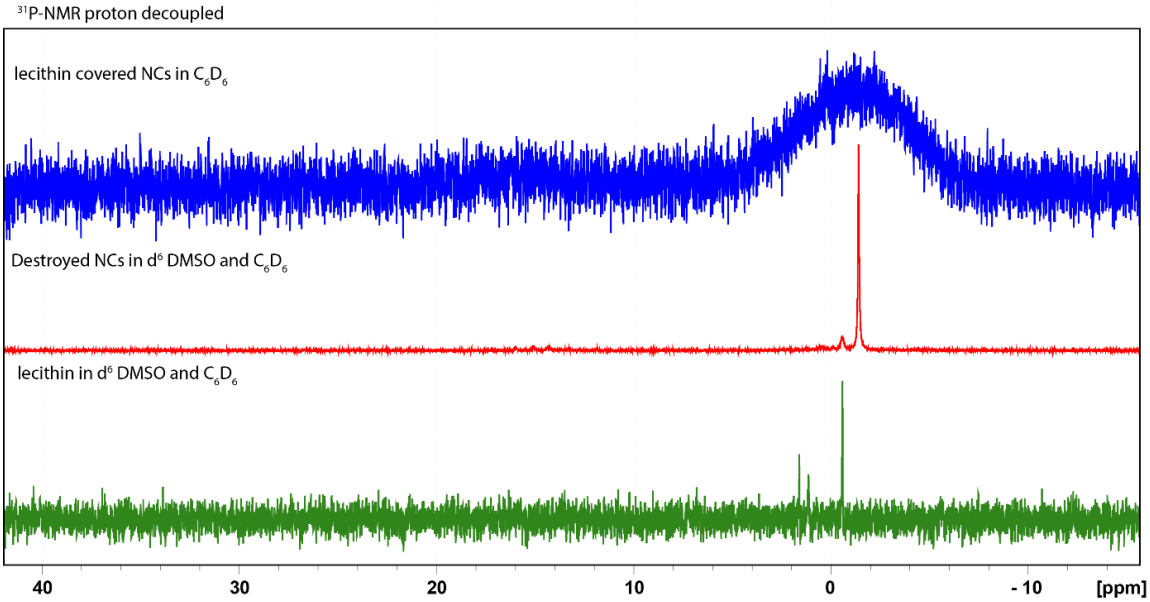

Figure S12. [31]P NMR of lecithin (green) and lecithin-covered NCs before (blue) and after dissolution (red) in d[6]-DMSO. The only phosphorous signal in the NC sample is the one from lecithin, showing pronounced broadening in the case of the NCs in benzene, which can be attributed to the much slower rotational correlation time of the phosphorous in the binding group; further line broadening mechanisms due to different environment and heterogeneous broadening cannot be excluded. Residual $TOPBr_2$ cannot be found, which agrees with the earlier observations with sulfobetaine ligands.[1]

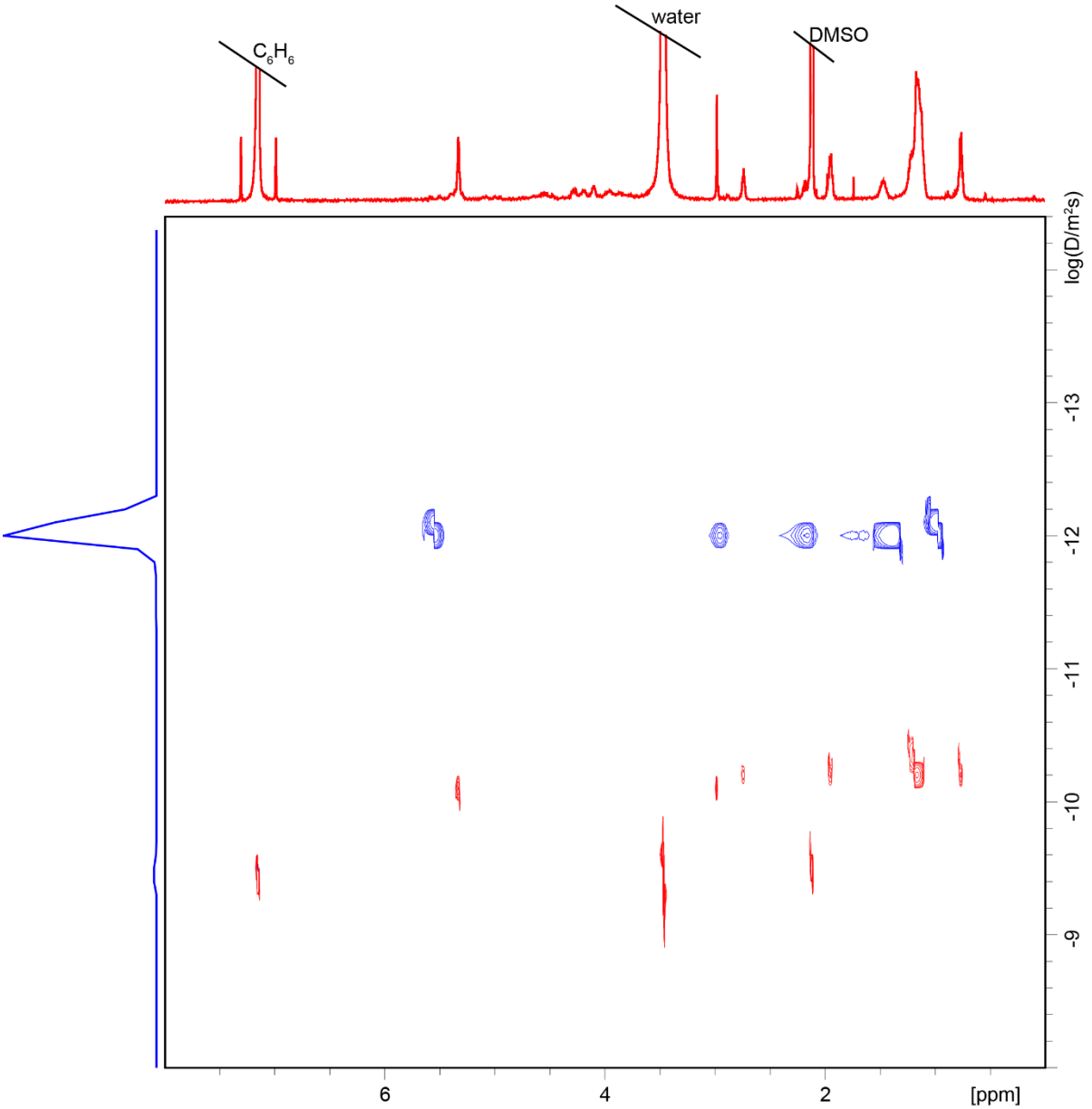

Figure S13. DOSY 2D spectra of lecithin in a mixture of C_6D_6 and DMSO d^6 (red) and lecithin-covered NCs (blue). The spectra have been laid one over the other. The x axis spectrum corresponds to dissolved lecithin in DMSO/Benzene. Notably the diffusion coefficient of the solvents is fastest followed by the diffusion coefficient of the free ligand and then by the diffusion coefficient of the NCs. Note that the extension in the y-direction is mostly due to lecithin being a mixture of molecules and probably also due to residual micelle formation, which can also explain the variation in the water and DMSO diffusion rates.

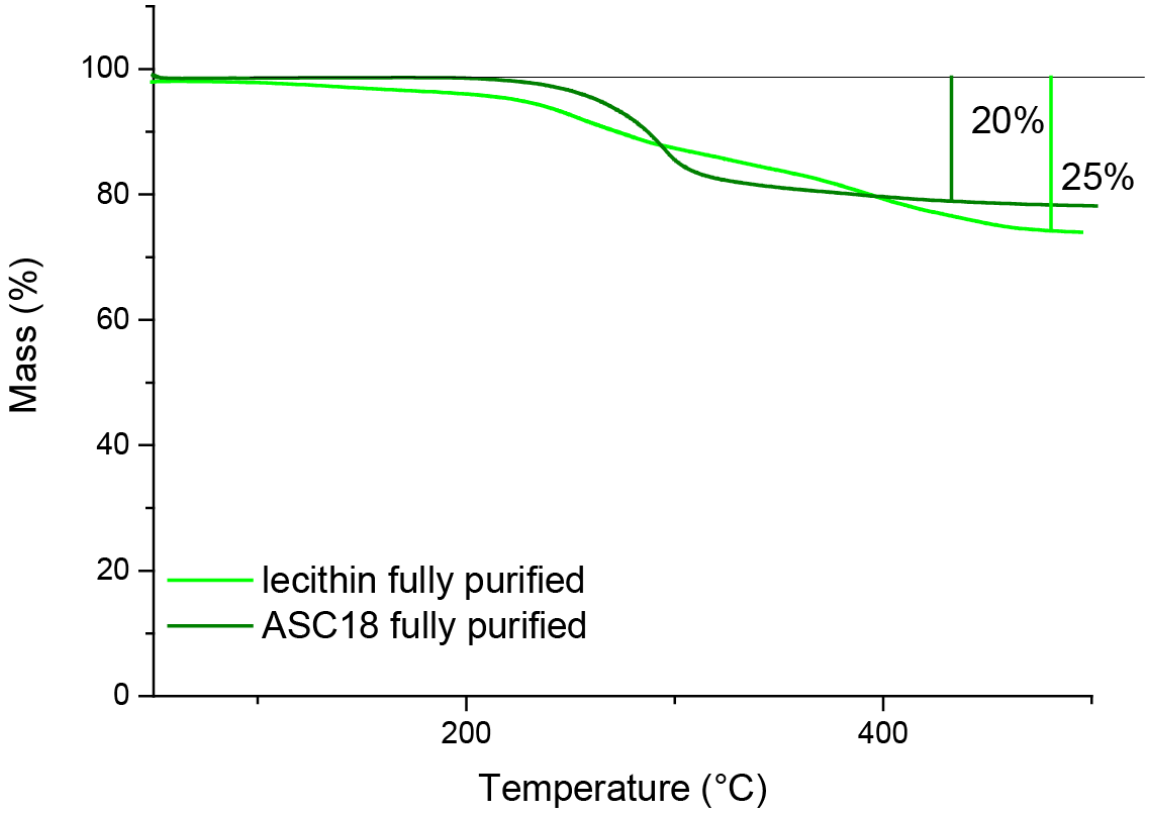

Figure S14. Thermogravimetric analysis (TGA) traces for different ligand systems. Lecithin enables same degree of purification as found in our earlier study on zwitterionic ligands such as sulfobetaine ASC18. [1] The higher TGA mass loss with lecithin-capping, which is a ligand mass fraction, is due to the higher ligand molecular mass. While 20% mass fraction in ASC18 corresponds to a coverage of 2 nm^{-2} or 72% of the surface sites, 25% mass fraction in lecithin converts to a coverage of 1.8 nm^{-2} or 64% of the surface sites.

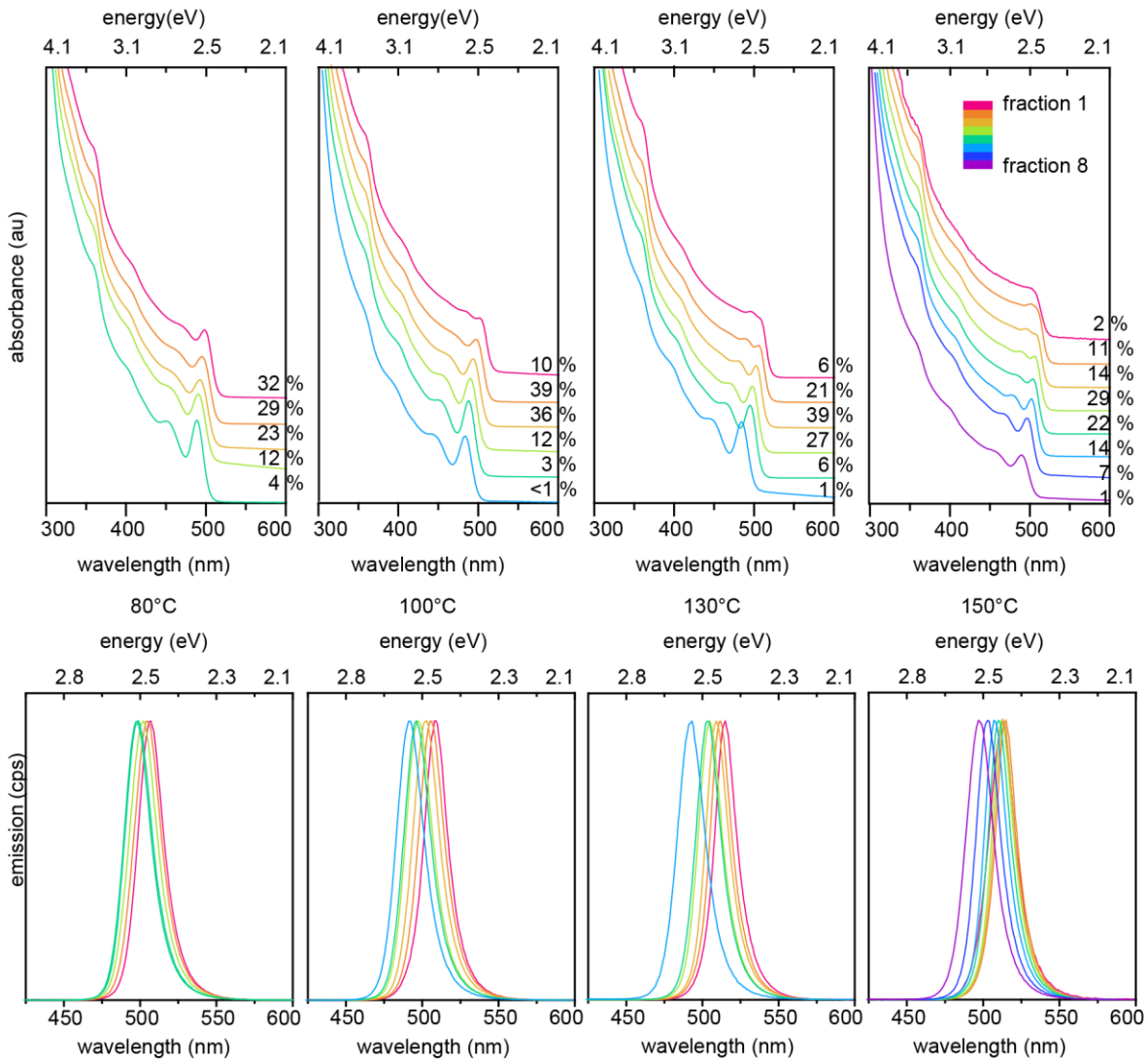

Figure S15. Absorption (top) and emission (bottom) spectra of fractions taken from lecithin-covered $CsPbBr_3$ NCs obtained by size-selective precipitation with acetone as an anti-solvent added in increments of 2 mL. Percentage next to the curves indicate the mass fraction. Note that the fractioning presented in Figure 3 employed anti-solvent increments of 1 mL, hence more fractions were isolated.

Table S3. Temperature dependence of the synthesis using lecithin as a ligand

Temperature	PL peak position for the smallest-NCs fraction	PL peak position for the dominant fraction (by weight)	PL peak position for the largest-NCs fraction
80 °C	492 nm (2.519 eV)	506 nm (2.446 eV)	506 nm (2.446 eV)
100 °C	498 nm (2.490 eV)	503 nm (2.467 eV)	509 nm (2.436 eV)
130 °C	504 nm (2.460 eV)	512 nm (2.421 eV)	515 nm (2.407 eV)
150 °C	503 nm (2.463 eV)	514 nm (2.413 eV)	515 nm (2.407 eV)

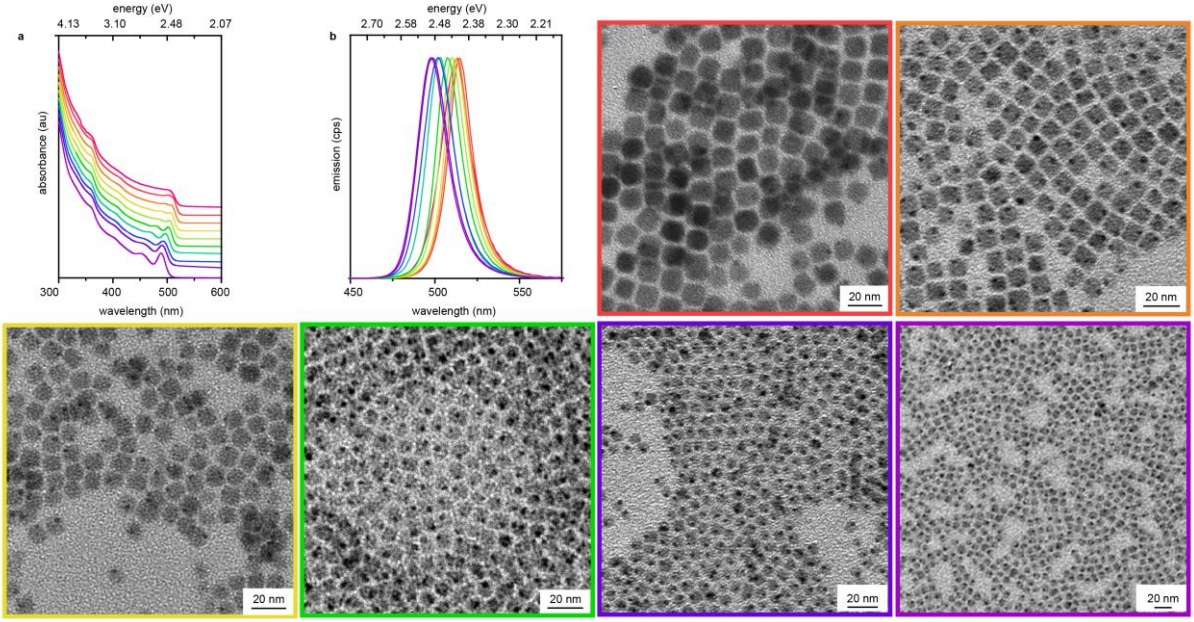

Figure S16. Selected (a) absorbance and (b) photoluminescence spectra of lecithin-covered $CsPbBr_3$ NCs of 6-10 nm edge length prepared by varying the temperature between 80 and 130 °C, followed by the size-selective precipitation. Color-coding of the curves correspond to the colors of the frames around the TEM images.

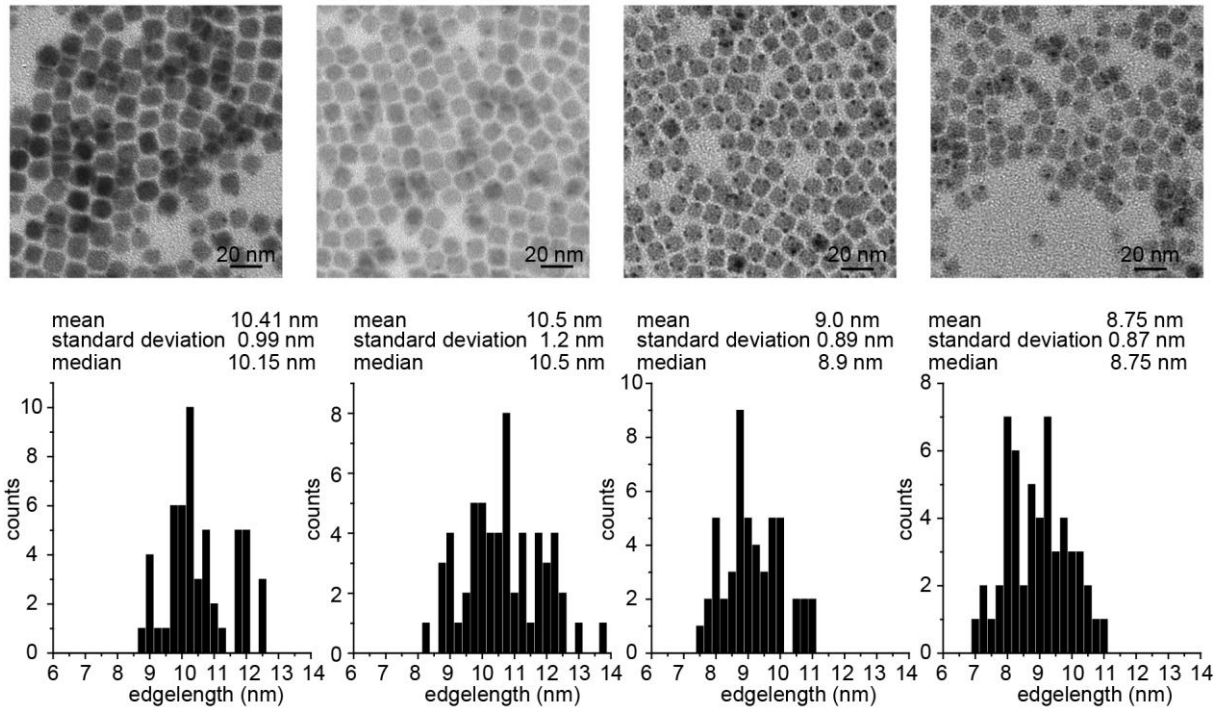

Figure S17. (Left to right) TEM images and corresponding size-histograms (edge-length) for fractions 6 to 9 (130 °C-synthesis), corresponding to the same samples as shown in Figure 3 of the main text.

4. Characterization

4.1 Optical characterization

Optical absorption UV-Vis absorption spectra for colloidal solutions were collected using a Jasco V670 spectrometer in transmission mode. A Fluorolog iHR 320 Horiba Jobin Yvon spectrofluorometer equipped with a PMT detector was used to acquire steady-state PL spectra from solutions. Absolute QY of films and solutions were measured with Quantaurus-QY Absolute PL quantum yield spectrometer from Hamamatsu. DLS measurements were performed on a Malvern Zetasizer Nano ZS in back scattering geometry, 12 acquisitions were performed per measurement and 3 measurements were taken per sample and temperature. For single NC spectroscopy, a home-built optical microscope was used. The sample was excited by a pulsed laser (70 W/cm^2, 10 MHz, laser emission at 405nm) which was focused ($1/e^2$=1 µm) by an oil immersion objective (NA=1.3). The emitted PL was collected by the same objective and sent to a monochromator coupled to an EMCCD camera. Alternately, the PL was sent to an HBT setup equipped with two APDs (time resolution=250 ps) for second order correlation measurements.

4.2 Materials characterization

XRD patterns were collected with STOE STADI P powder diffractometer, operating in transmission mode. A germanium monochromator, Cu Kα1 irradiation and a silicon strip detector (Dectris Mythen) was used. TGA and DSC were performed using a Netzsch Simultaneous Thermal Analyzer (STA 449 F5 Jupiter). A powdered sample (ca. 20 mg) was placed in an alumina crucible and heated under Ar gas flow (50 ml/min) to 500 °C (5 °C min^{-1}). TEM images were collected using Hitachi HT7700 microscope operated at 100 kV and a JEOL JEM-2200FS microscope operated at 200 kV. TEM images were processed using Fiji [15]. HAADF-STEM images were collected at cryo-conditions (holder cooled with liquid nitrogen) on a Tecnai F30 (Thermo Fisher Scientific) operated at 300 kV with a point resolution of *ca*. 2 Å. SEM images were acquired with a FEI Quanta 200F at 100 kV in Z-contrast mode. Atomic-force-microscopy images were recorded with a Bruker Dimension Icon in PeakForce Tapping mode and Scanasyst-Air cantilever.

4.3 NMR spectroscopy

Spectra of NCs dispersions and decomposed NC dispersions as well as DOSY spectra were measured on a Bruker Avance III HD Spectrometer operating at a ^{1}H frequency of 500.26 MHz and equipped with a BBFO-Z probe. The sample temperature was set to 298.2 K.

NMR samples were purified using benzene and acetone and 4 washing steps. The resulting precipitate after the fourth washing step was dried to powder under vacuum and subsequently dispersed in 0.6 mL of benzene (d6) and centrifuged at 1337 g for 10 min. In order to be certain about colloidal stability of the NMR sample it was usually measured 12 to 24 h after preparation. The NCs were dissolved (decomposed) by adding 0.6 mL of DMSO (d6) directly to the NMR tube in order to liberate the ligands from the surface. This solvent was chosen since it dissolves the ligands as well as bulk $CsPbX_3$ (X= Cl, Br). The resulting solution was a colorless transparent solution of ions, ligands and solutes, which had been present in the NC dispersion.

Diffusion measurements were performed on $CsPbBr_3$ NC using a double stimulated echo sequence (for convection compensation) with monopolar gradient pulses [16]. Smoothed rectangle gradient pulse shapes were used throughout. The gradient strength was varied linearly from 2 to 95% of the probe's maximum value in 32 or 64 increments, with the gradient pulse duration and diffusion delay optimized to ensure a final attenuation of the signal in the final increment of less than 10% relative to the first increment. The spectra were fitted to the Stejskal-Tanner equation [17] using the topspin relaxation module. The diffusion coefficient could be related to the NC size and *vice versa* by the Stokes Einstein equation:

$$D = k_B T 6 \pi \eta c a$$

where k_B is the Boltzmann constant, T - the temperature, η - the viscosity of the solvent (Benzene, the viscosity of the solution does not deviate at small volume loadings), c - a shape factor for the cubic shape (0.66) and a - the edge length of the NC.

4.4 Analytical ultra-centrifugation (AUC)

All sedimentation velocity measurements were performed with a Beckman Coulter Optima XL-I analytical ultracentrifuge equipped with an AN-50 rotor. Two-sector cells (path length 12 mm) comprising a titanium centerpiece (Nanolytics) and sapphire windows were used. A concentrated dispersion of each NC fraction was diluted in toluene to yield an absorbance of about 1 OD at a chosen recording wavelength (equivalent to 16 mg/mL for collection at 335 nm and 80 mg/mL for collection at 500 nm). The AUC was stabilized at least 1 hour prior to

measurement. All experiments were conducted at 20 °C at a speed in the range from 5000 – 10000 rpm, and no delay was set in between scans.

Sedfit (version 16.1c) was used to fit the radial profiles with Lamm's equation solutions, from which the distribution of sedimentation coefficients C(*s*) and C(*s*, f/f_0) were calculated. For C(*s*), the *s* range was set to 100 - 2000 Svedberg units with the resolution of 100 steps. The weighted average solvo-dynamic particle size and core size were estimated using the reported method in reference [18] under the assumption that the particles are spherical. The other assumptions are the bulk density of core (4.80 g/cm^3) [11] and bulk density of lecithin (1.41 g/cm^3). For this calculation, the C(*s*,f/f_0) took the *s* range from 100-2000 in 100 steps and frictional ratio f/f_0 from 0.1-4 in 20 steps. In this model, the C(s) was calculated assuming the particle density to be the same as the bulk density of the core. The frictional ratio f/f_0, meniscus, and noise were fitted. The assumed particle density was set when the value of f/f_0 was closed to 1.05 which is the f/f_0 of a cube. C(*s*,f/f_0) was evaluated for the 2D distribution in essentially a model independent way. The result was processed by the Matlab script reported earlier [19]. To assert the quality of the particles C(*s*) from radial profiles at lower wavelength of 335nm, and interferograms was also calculated. The fitting plots were prepared by GUSSI.

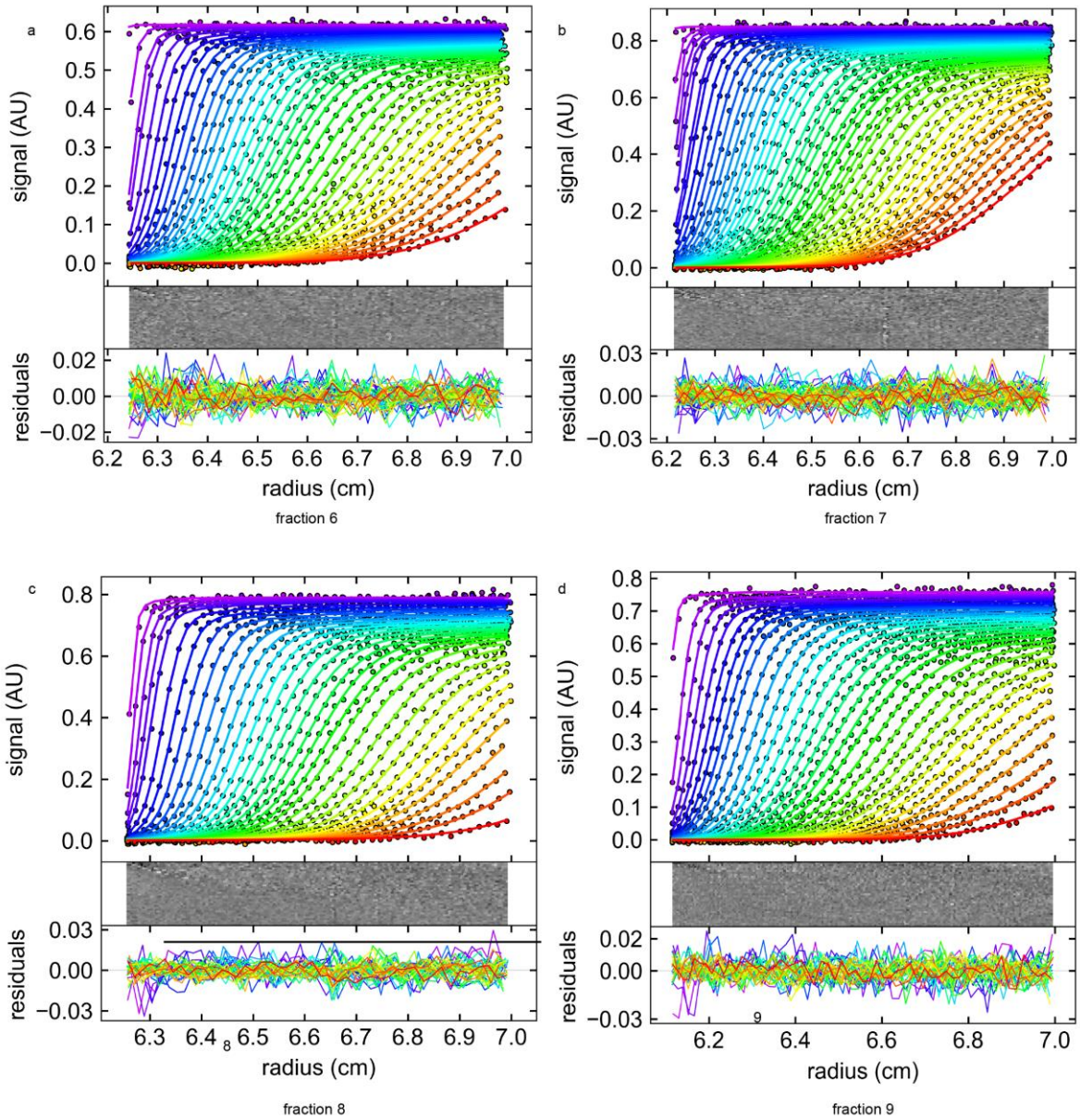

Figure S18. (a)-(d) Sedimentation curves for fractions 6-9 respectively. Data were collected at 500 nm absorbance and fitted with the Lamm's equation. (Top panel) points are measured data points colored lines are best fits. (Middle panel) the fitting residual image. (Lower panel) residual plots of the fit.

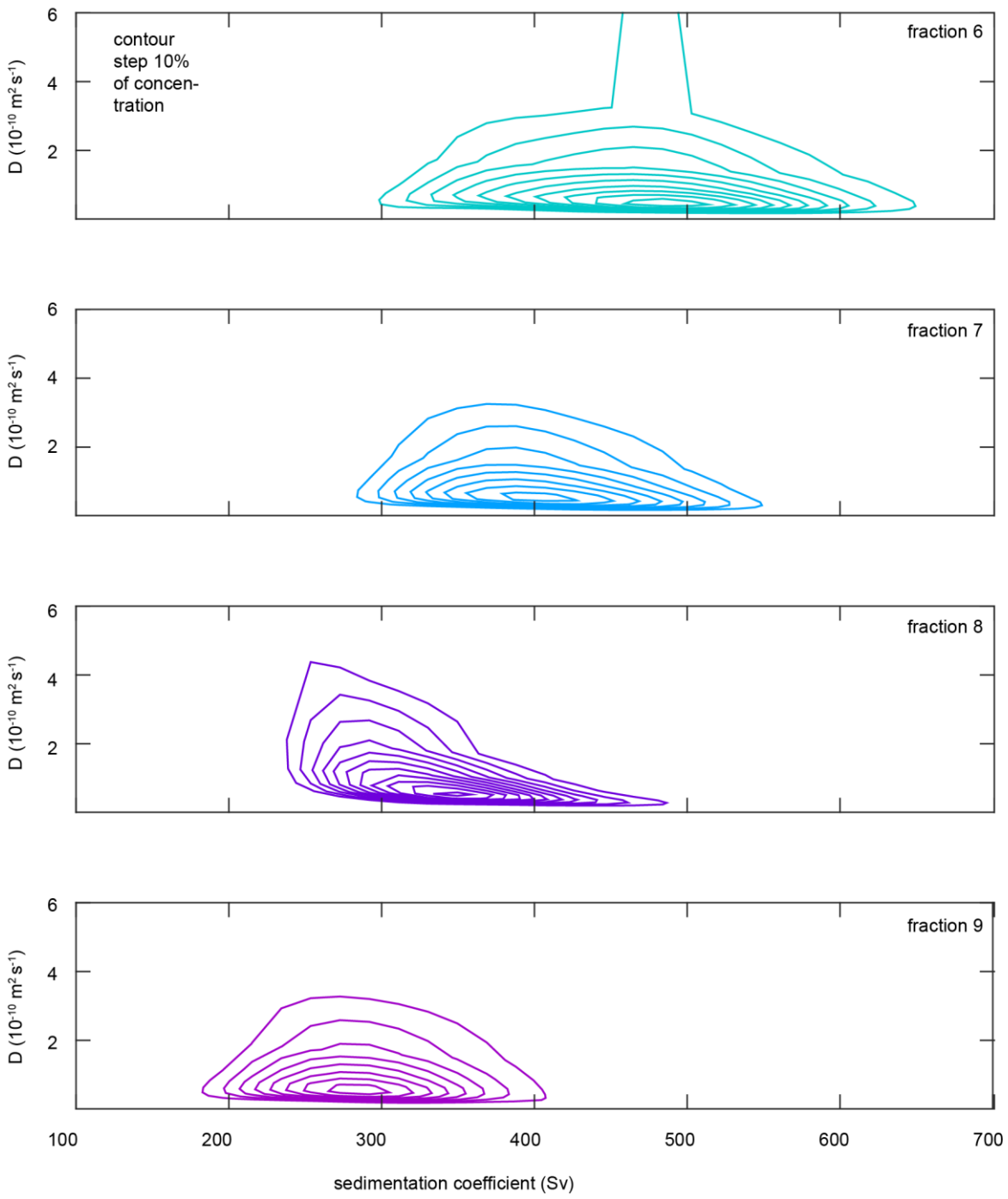

Figure S19. The C(s,D) distributions estimated by Sedfit from absorbance scans at 500nm for fractions 6, 7, 8, and 9. From the distributions, solvo-dynamic particle size and core size were calculated and tabulated in Table S4.

Table S4. Weight averaged sedimentation and diffusion coefficients calculated from C(s, D) for each fraction, from which the hydrodynamic diameters and core diameters were estimated. Density of $CsPbBr_3$ = 4.796 g/cm^3, density of ligands = 1.41 g/cm^3.

fraction number	D (m^2/s)	s (10^{-13})	Solvo-dynamic diameter (nm) sphere model	Solvo-dynamic diameter (nm) cuboid model	core edge length (nm) sphere model	core edge length (nm) cuboid model	density (g/cm^3)	vbar (cm^3/g)
6	6.02061E-11	482.64	12.1	13.7	9.5	10.3	4.3742	0.2286
7	5.9359E-11	414.05	12.3	13.3	8.9	9.6	3.7917	0.2637
8	6.38E-11	351.81	11.4	11.7	8.1	8.7	3.7377	0.2675
9	6.13E-11	292.33	11.9	11.6	7.5	8.0	3.0666	0.3261

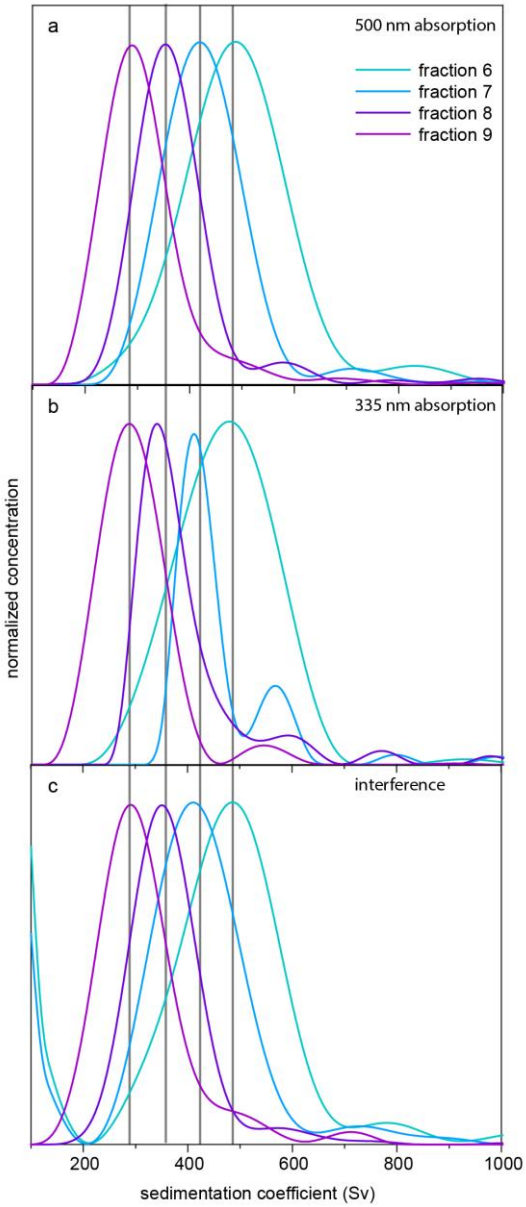

Figure S20.. The comparison of normalized sedimentation coefficient distributions of fractions 6-9: (a) from absorbance scans using the wavelength of 500 nm; (b) from absorbance scans using the wavelength of 335 nm; (c) from interferograms recording simultaneously with the absorbance scans of 500 nm. The rise towards low sedimentation coefficients in panel (c) is an artifact because of the residual background of the interference profiles.

4.5 Small angle X-Ray Scattering (SAXS)

Methods:

Small angle X-ray scattering**.** Small angle x-ray scattering (SAXS) measurements were performed at the Austrian SAXS beamline of the electron storage ring ELETTRA using a photon energy of 8 keV [20]. The beamline setup was adjusted to a sample to detector distance of 780 mm to result in an accessible q-range 0.12–8.5 nm^{-1}. All images were recorded using the Pilatus 1M detector (Dectris, Switzerland) with 20 exposures of 5 seconds per sample to check for radiation damage. Reference patterns to calibrate the q-scale were collected of silver-behenate (*d*-spacings of 5.838 nm). All measurements were done using a 1.5 mm quartz flow cell capillary. The radial averaging and the image calibration were conducted using the FIT2D software [21]. All presented data was corrected for fluctuations of the primary intensity and the corresponding background (toluene) has been subtracted from each scattering pattern after transmission correction.

SAXS model fitting

Scattering patterns were fitted using (a) an analytical model and (b) the model-free SASHEL Monte Carlo algorithm. The results of both approaches are consistent with each other, yielding a non-cubic but orthorhombic nanocrystal shape. The methodological details on both fitting approaches are described in the following.

Analytical model: The scattering intensity $I_{an}(q)$ of the analytical model corresponds to polydisperse (Gaussian volume-distribution), orthorhombic parallelepipeds and is written as

$$I_{an}(q) = BG + I_0 \cdot \sum_i^{N_{SD}} G(r_i, a, \sigma) \cdot V \cdot F\left(q, r_i, \frac{b}{a}, \frac{c}{a}\right) \qquad (4)$$

where BG denotes a constant residual background and I_0 denotes the forward scattering intensity scalar. The fitting parameters are: (a) the first (smallest) NC side length, ($\frac{b}{a}$) the aspect ratio of the second to first NC side length, ($\frac{c}{a}$) the aspect ratio of the third to first NC side length and (σ) the standard-deviation of the size-distribution (relative) [22]. The summation part of the equation represents the numerical average over the Gaussian distribution $G(r_i, a, \sigma)$, here consisting of N_{SD} = 51 discrete points. The size distribution is calculated over the range $a(1-3\sigma) < r_i < a(1+3\sigma)$ and is weighted by volume $V = r_i^3 \cdot \frac{b}{a} \cdot \frac{c}{a}$. We calculate the formfactor contribution $F\left(q, r_i, \frac{b}{a}, \frac{c}{a}\right)$ describing the orthorhombic NC shape according to literature [23] such that $F(q=0) = 1$, where r_i denotes the shortest NC side length corresponding to the respective size-distribution weight such that the other sides are scaled by $\frac{b}{a}$ and $\frac{c}{a}$. Fitting results can be found in Table S5 – the model patterns are shown in Figure 4 and Figure S21)

First, scattering patterns were fitted using the "orthorhombic polydisperse" model by optimizing all parameters but keeping the background (BG) fixed (value was estimated from a power law fit of the high q data). For both samples, we are able to refine the full scattering pattern with very good agreement (see black traces in Figure 4 and Figure S21), as quantified by the goodnesss-of-fit value $\chi^2 < 1.6$. To visualize the scattering contribution coming only from the NC shape and not from the size-distribution, we used the refined shape parameters and assumed perfect monodispersity for the calculation of the "orthorhombic monodisperse" model. As validation that the obtained NC shape is indeed orthorhombic and not cubic, we performed the same full pattern refinement but assuming an aspect ratio of $\frac{b}{a} = \frac{c}{a} = 1$. As seen under "cubic polydisperse" model, we find worse agreement of model and experimental scattering pattern, as evidenced by (i) stronger oscillations in the fitting residuals (see Figure 4 and Figure S21) and (ii) a higher and hence worse χ^2 value (Table S5).

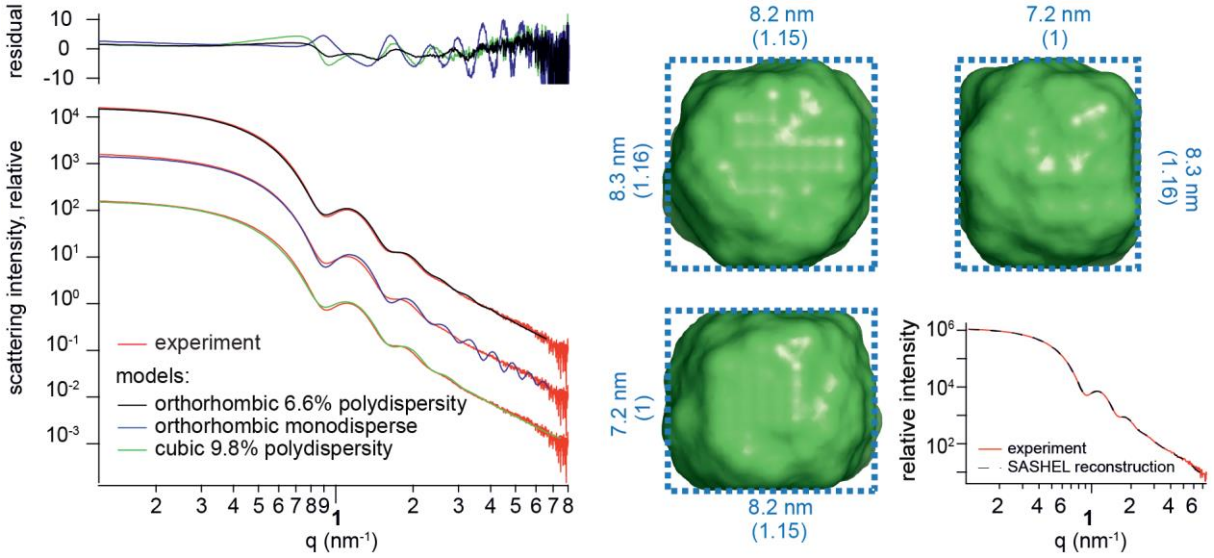

Figure S21. (Left) SAXS traces of NCs from fraction 9 (red) fitted with a monodisperse orthorhombic (blue) and polydisperse cubic (green) and orthorhombic (black) models. Best fit was found for an orthorhombic model with 6.6 % polydispersity on the edge lengths. (Right) Model free 3D reconstruction from the small angle scattering data along with the resulting NC shape, shown from 3 sides.

Table S5. Optimized fitting parameters of the SAXS full pattern refinement. For an explanation of the variables, see eq. (4) and the description above. Grey cells denote parameters that have been set as fixed during the fitting process. . The error gives the mean relative uncertainty of each fitting parameter, as determined from covariance analysis weighted by the experimental error band.

		fraction 8			**fraction 9**			
		ortho. polydisp.	**ortho. monodisp.**	**cubic polydisp.**	**ortho. polydisp.**	**ortho. monodisp.**	**cubic polydisp.**	**Error [%]**
BG	[.]	0.008	0.008	0.008	0.008	0.008	0.008	-
I_0	[.]	10.38	12.59	4.53	10.68	12.83	4.76	3.22
a	[nm]	7.99	7.99	8.67	7.27	7.27	7.90	4.14
b/a	[1]	1.16	1.16	1.00	1.17	1.17	1.00	6.11
c/a	[1]	1.16	1.16	1.00	1.17	1.17	1.00	5.98
σ	[%]	6.43	0.00	9.42	6.61	0.00	9.77	5.43
χ^2	[.]	**1.47**	**5.48**	**2.51**	**1.61**	**5.42**	**4.30**	

Model-free reconstruction: As a verification of the chosen analytical model and the obtained fitting results, we performed a model-free Monte Carlo 3D reconstruction of the NC shape using the SASHEL program [24]. While this approach assumes perfect monodispersity, it has previously been shown that size-distributions below $\sigma < 10\%$ have a negligible effect on the reconstructed shape [25]. Scattering patterns were fitted over 150 iterations starting from a movement temperature of 0.5 and a cubic shape of 7.5 nm for both samples. For each sample, we performed 8 independent reconstructions, which were subsequently aligned, superimposed and merged for statistical analysis using DAMAVER [26]. For both samples, and in agreement with the analytical model, we find (i) a non-cubic but orthorhombic shape and (ii) NC dimensions that are almost identical to the analytical model (see Figure 4 and Figure S21).

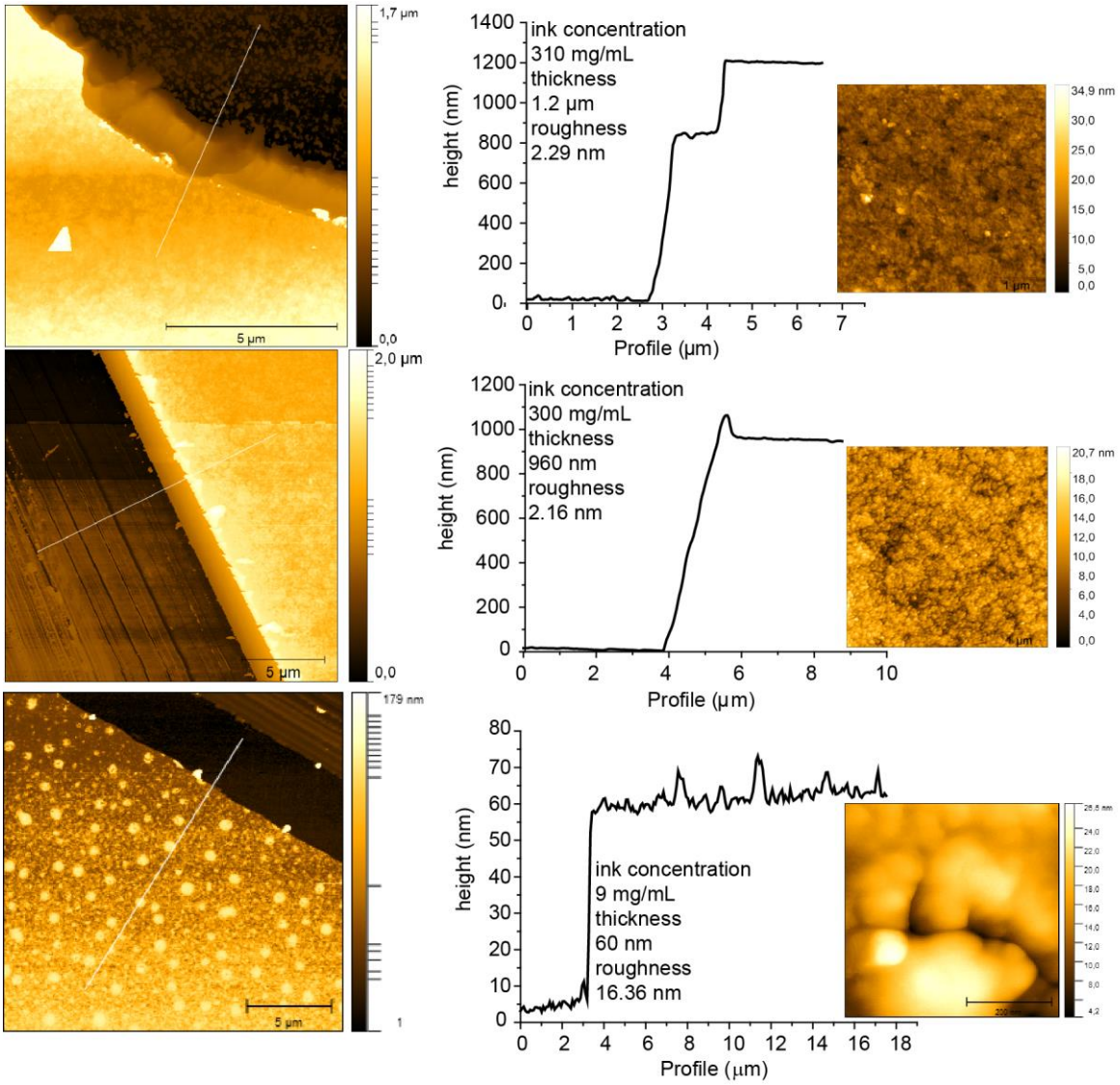

Figure S22. (left) Selected AFM images of scratched films made from toluene solutions of lecithin capped $CsPbBr_3$ NCs ordered by decreasing ink concentration (top to bottom). The scale is logarithmic to show the film structure in detail. (middle) The profile plots along the white line in the image on the left. (right) High-resolution scans. The roughness listed is the root mean square roughness of the high-resolution images. The roughness used in Figure 5a is the difference between the highest and the lowest point in the high-resolution image (peak-to-peak roughness). From the high-resolution images of the two thickest films, it can be seen that the NCs remain largely intact and do not sinter into large entities.

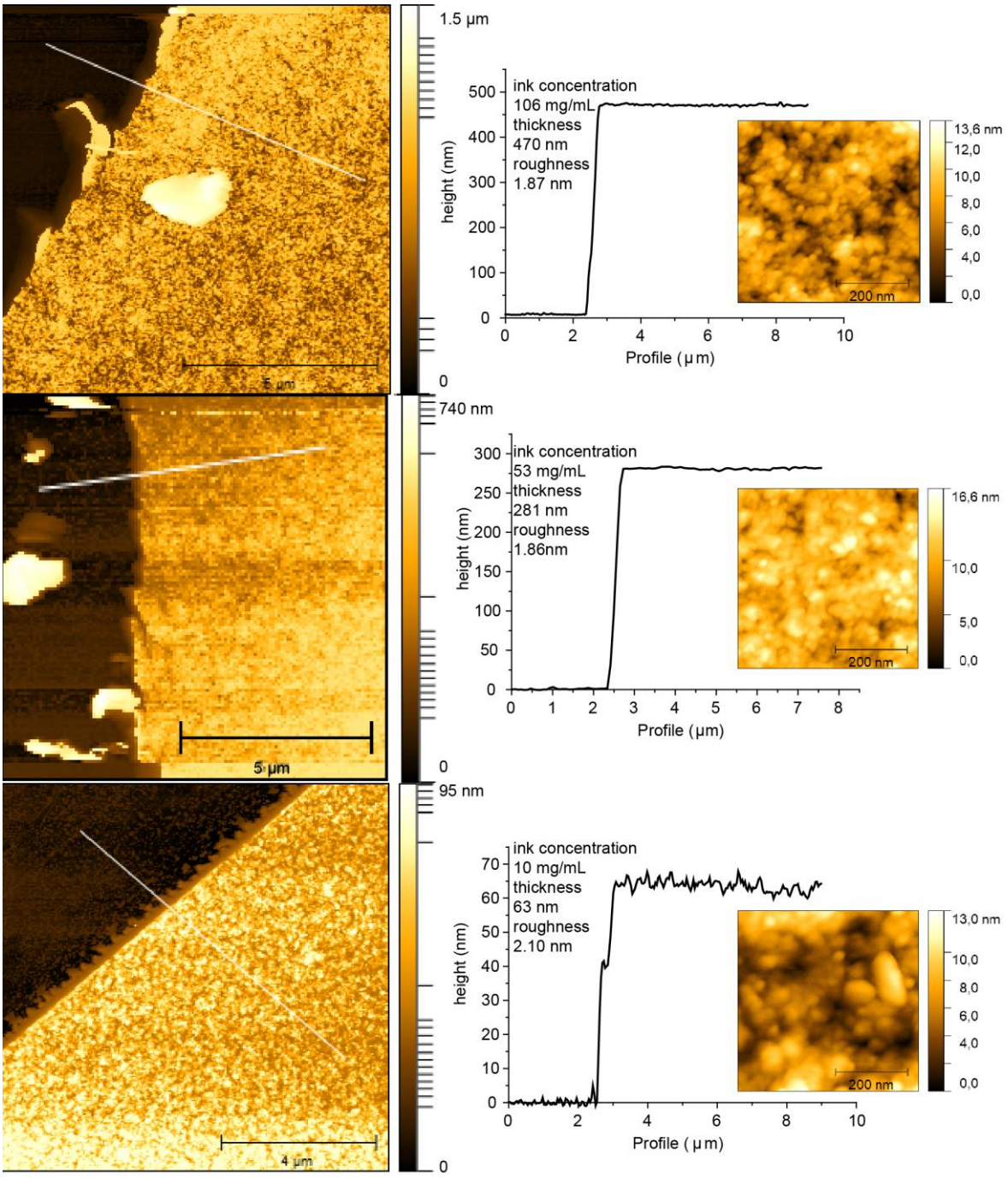

Figure S23. (left) Selected AFM images of scratched films made from toluene solutions of ASC18 capped $CsPbBr_3$ NCs ordered by decreasing ink concentration (top to bottom). The scale is logarithmic to show the film structure in detail. (middle) The profile plots along the white line in the image on the left. (right) High resolution scans the roughness listed is the root mean square roughness of the high-resolution images. The roughness used in Figure 5a is the difference between the highest and the lowest point in the high-resolution image. From the high-resolution images, it can be seen that the NCs remain largely intact and do not sinter into large entities.

5. Literature

1. Krieg, F.; Ochsenbein, S. T.; Yakunin, S.; Ten Brinck, S.; Aellen, P.; Suess, A.; Clerc, B.; Guggisberg, D.; Nazarenko, O.; Shynkarenko, Y.; Kumar, S.; Shih, C. J.; Infante, I.; Kovalenko, M. V., Colloidal $CsPbX_3$ (X = Cl, Br, I) Nanocrystals 2.0: Zwitterionic Capping Ligands for Improved Durability and Stability. *ACS Energy Lett.* **2018**, *3*, 641-646.
2. (a) De Gennes, P. G., Polymers at an interface; A simplified view *Adv. Colloid Interface Sci.* **1987**, *27*, 189-209; (b) De Gennes, P. G., Polymers at an Interface. 2. Interaction between two Plates Carrying Adsorbed Polymer Layers. *Macromolecules* **1982**, *15*, 492-500.
3. (a) Milner, S. T., Strongly Stretched Polymer Brushes. *J. Polym. Sci. Pol. Phys.* **1994**, *32*, 2743-2755; (b) Milner, S. T.; Witten, T. A.; Cates, M. E., Theory of the Grafted Polymer Brush. *Macromolecules* **1988**, *21*, 2610-2619; (c) Milner, S. T.; Witten, T. A.; Cates, M. E., A Parabolic Density Profile for Grafted Polymers. *Europhys. Lett.* **1988**, *5*, 413-418.
4. (a) Chen, C. M.; Fwu, Y. A., Monte Carlo Simulations of Polymer Brushes. *Phys. Rev. E Stat. Nonlin. Soft Matter Phys.* **2001**, *63*, 011506; (b) Cosgrove, T.; Heath, T.; van Lent, B.; Leermakers, F.; Scheutjens, J., Configuration of Terminally Attached Chains at the Solid/Solvent Interface: Self-Consistent Field Theory and a Monte Carlo Model. *Macromolecules* **1987**, *20*, 1692-1696; (c) Chakrabarti, A.; Toral, R., Density Profile of Terminally Anchored Polymer Chains: A Monte Carlo Study. *Macromolecules* **1990**, *23*, 2016-2021; (d) Murat, M.; Grest, G. S., Interaction between Grafted Polymeric Brushes: A Molecular-Dynamics Study. *Phys. Rev. Lett.* **1989**, *63*, 1074-1077; (e) Muthukumar, M.; Ho, J.-S., Self-Consistent Field Theory of Surfaces with Terminally Attached Chains. *Macromolecules* **1989**, *22*, 965-973; (f) Scheutjens, J. M. H. M.; Fleer, G. J., Statistical Theory of the Adsorption of Interacting Chain Molecules. 1. Partition Function, Segment Density Distribution, and Adsorption Isotherms. *J. Phys. Chem.* **1979**, *83*, 1619-1635; (g) Milner, S. T., Strong-stretching and Scheutjens-Fleer Descriptions of Grafted Polymer Brushes. *J. Chem. Soc. Faraday Trans.* **1990**, *86*, 1349-1353.
5. Spiliopoulos, N.; Koutsioubas, A. G.; Anastassopoulos, D. L.; Vradis, A. A.; Toprakcioglu, C.; Menelle, A.; Mountrichas, G.; Pispas, S., Neutron Reflectivity Study of Free-End Distribution in Polymer Brushes. *Macromolecules* **2009**, *42*, 6209-6214.
6. De Roo, J.; Ibanez, M.; Geiregat, P.; Nedelcu, G.; Walravens, W.; Maes, J.; Martins, J. C.; Van Driessche, I.; Kovalenko, M. V.; Hens, Z., Highly Dynamic Ligand Binding and Light Absorption Coefficient of Cesium Lead Bromide Perovskite Nanocrystals. *ACS Nano* **2016**, *10*, 2071-81.
7. (a) Israelachvili, N. J., Repulsive "Steric" or "Overlap" Forces between Polymer-Covered Surfaces. In *Intermolecular and Surface Forces*, 3 ed.; Elsevier: 2011; pp 387-393; (b) Manciu, M.; Ruckenstein, E., Simple Model for Grafted Polymer Brushes. *Langmuir* **2004**, *20*, 6490-6500.
8. Marsh, D., Calorimetric Data. In *Handbook of lipid bilayers*, 2 ed.; CRC Press: 2013; pp 297-.
9. (a) Yang, Y.; Qin, H.; Peng, X., Intramolecular Entropy and Size-Dependent Solution Properties of Nanocrystal-Ligands Complexes. *Nano Lett.* **2016**, *16*, 2127-2132; (b) Yang, Y.; Qin, H.; Jiang, M.; Lin, L.; Fu, T.; Dai, X.; Zhang, Z.; Niu, Y.; Cao, H.; Jin, Y.; Zhao, F.; Peng, X., Entropic Ligands for Nanocrystals: From Unexpected Solution Properties to Outstanding Processability. *Nano Lett.* **2016**, *16*, 2133-2138.
10. Milner, S. T.; Witten, T. A.; Cates, M. E., Effects of Polydispersity in the End-Grafted Polymer Brush. *Macromolecules* **1989**, *22*, 853-861.
11. Bertolotti, F.; Protesescu, L.; Kovalenko, M. V.; Yakunin, S.; Cervellino, A.; Billinge, S. J. L.; Terban, M. W.; Pedersen, J. S.; Masciocchi, N.; Guagliardi, A., Coherent Nanotwins and Dynamic Disorder in Cesium Lead Halide Perovskite Nanocrystals. *ACS Nano* **2017**, *11*, 3819-3831.
12. Maes, J.; Balcaen, L.; Drijvers, E.; Zhao, Q.; De Roo, J.; Vantomme, A.; Vanhaecke, F.; Geiregat, P.; Hens, Z., Light Absorption Coefficient of $CsPbBr_3$ Perovskite Nanocrystals. *J. Phys. Chem. Lett.* **2018**, *9*, 3093-3097.
13. Protesescu, L.; Yakunin, S.; Bodnarchuk, M. I.; Krieg, F.; Caputo, R.; Hendon, C. H.; Yang, R. X.; Walsh, A.; Kovalenko, M. V., Nanocrystals of Cesium Lead Halide Perovskites ($CsPbX_3$, X = Cl, Br, and I): Novel Optoelectronic Materials Showing Bright Emission with Wide Color Gamut. *Nano Lett.* **2015**, *15*, 3692-6.
14. Moller, C. K., Crystal structure and photoconductivity of cesium plumbohalides. *Nature* **1958**, *182*, 1436.

15. Schindelin, J.; Arganda-Carreras, I.; Frise, E.; Kaynig, V.; Longair, M.; Pietzsch, T.; Preibisch, S.; Rueden, C.; Saalfeld, S.; Schmid, B.; Tinevez, J.-Y.; James White, D. J.; Hartenstein, V.; Eliceiri, K.; Tomancak, P., Fiji: an open-source platform for biological-image analysis. *Nat. Methods* **2012**, *9*, 676–682.
16. Connell, M. A.; Bowyer, P. J.; Adam Bone, P.; Davis, A. L.; Swanson, A. G.; Nilsson, M.; Morris, G. A., Improving the accuracy of pulsed field gradient NMR diffusion experiments: Correction for gradient non-uniformity. *J. Magn. Reson.* **2009**, *198*, 121-131.
17. Sinnaeve, D., The Stejskal-Tanner Equation Generalized for any Gradient Shape-an Overvies of most pulse sequences measuring free diffusion. In *Concepts Mag. Reson.*, 2012; Vol. Part A, pp 39-65.
18. Carney, R. P.; Kim, J. Y.; Qian, H.; Jin, R.; Mehenni, H.; Stellacci, F.; Bakr, O. M., Determination of Nanoparticle Size Distribution Together with Density or Molecular Weight by 2D Analytical Ultracentrifugation. *Nat. Commun.* **2011**, *2*, 335-343.
19. Carney, R. P.; Kim, J. Y.; Qian, H.; Jin, R.; Mehenni, H.; Stellacci, F.; Bakr, O. M., Determination of nanoparticle size distribution together with density or molecular weight by 2D analytical ultracentrifugation. *Nat Commun* **2011**, *2*, 335.
20. Amenitsch, H.; Bernstorff, S.; Laggner, P., High-flux beamline for small-angle x-ray scattering at ELETTRA. *Rev. Sci. Instrum.* **1995**, *66*, 1624-1626.
21. Hammersley, A. P.; Svensson, S. O.; Thompson, A.; Graafsma, H.; Kvick, Å.; Moy, J. P., Calibration and Correction of Distortions in Two-Dimensional Detector Systems. *Rev. Sci. Instrum.* **1995**, *66*, 2729-2733.
22. Glatter, O., Determination of Particle-size Distribution Functions from Small-Angle Scattering Data by means of the Indirect Transformation Method. *J. Appl. Crystallogr.* **1980**, *13*, 7-11.
23. Pedersen, J. S., analysis of small-angle scattering data from colloids and polymer solutions: modeling and least squares fitting. *Adv. Colloid Interface Sci.* **1997**, *70*, 171-210.
24. Burian, M.; Amenitsch, H., Dummy-atom modelling of stacked and helical nanostructures from solution scattering data. *IUCRJ* **2018**, *5*, 390-401.
25. Burian, M.; Fritz-Popovski, G.; He, M.; Kovalenko, M. V.; Paris, O.; Lechner, R. T., Considerations on the Model-Free Shape Retrieval of Inorganic Nanocrystals from Small-Angle Scattering Data. *J. Appl. Crystallogr.* **2015**, *48*, 857-868.
26. Volkova, V. V.; Svergunb, D. I., Uniqueness of ab initio shape determination in small-angle scattering *J.Appl.Cryst.* **2003**, *36*, 860-864.